KU LEUVEN

FACULTEIT WETENSCHAPPEN

Development of a saturated absorption spectroscopy setup at IGISOL

Sarina GELDHOF

Promotor: Prof. Dr. G. Neyens
Co-promotor: Dr. A. Voss (University of Jyväskylä)
Begeleider: H. Heylen

Proefschrift ingediend tot het behalen van de graad van Master of Science in de Fysica

Academiejaar 2014-2015

Dankwoord

Het dankwoord: traditioneel het laatste hoofdstuk dat geschreven wordt, maar daarom niet minder belangrijk. Eerst en vooral wil ik mijn promotor Prof. Gerda Neyens bedanken voor de steun gedurende het hele jaar. Het feit dan deze thesis deels in Finland, deels in Leuven tot stand is gekomen zorgde niet altijd voor de gemakkelijkste manier van werken, maar dankzij uw begeleiding is alles vlot verlopen. Bedankt voor uw geduld en de open manier van werken en communiceren.

A big thank you to my second promotor, Dr. Annika Voss, for all the support this year. Thanks for the great guidance at the lab, your patience and willingness to include me in everything have made it a very instructive and pleasant exchange semester. Thanks as well for all the help by e-mail during the second semester. I would like to thank all the other people at IGISOL, especially Iain Moore and Paul Campbell, for welcoming me in the group, taking the time to explain things to me and including me in the experiments. A special thanks to Chantal and Michael for the great times in the lab and out in the city. I would like to thank Bradley Cheal to let me participate in the collinear laser spectroscopy experiment. Even though it didn't work out as planned, I still learned a lot.

Bedankt aan mijn kantoorgenoten in het tweede semester, Hanne, Wouter en Ivan, voor de hulp bij kleine en grote (Python) problemen en de leuke sfeer.

Thanks to everyone who made my Erasmus exchange in Jyväskylä so amazing. It's impossible to thank everyone here, but I would like to mention my tutor Milla. You were a great tutor and made our 'tutor group' a real group of friends. A big thank you of course to all my friends in Leuven as well to make the other 4.5 years the best time of my life.

Merci Heleen, voor je nuchtere blik op alles die ik af en toe goed kan gebruiken, en natuurlijk om de beste zus te zijn. En last but not least, bedankt mama en papa voor jullie niet-aflatende steun. Ik liet het misschien niet altijd genoeg blijken, maar ik besef zeker wat een geschenk dit vijf jaar durend avontuur is geweest.

Samenvatting

Deze thesis presenteert de karakterisatie van een gesatureerde absorptie spectroscopie opstelling aan de IGISOL faciliteit van de universiteit van Jyväskylä, waar het onderzoek voor deze thesis werd uitgevoerd in het kader van een Erasmus uitwisseling van één semester. De doelstelling van deze opstelling in het kader van hoge-resolutie laser spectroscopie metingen, alsook de onderliggende theoretische achtergrond van deze techniek en een gedetailleerde beschrijving van de opstelling wordt gepresenteerd. De manier waarop de spectra verkregen van gesatureerde absorptie spectroscopie van rubidium afhangen van het vermogen van de laser wordt bestudeerd. De Fabry-Perot interferometer die een onderdeel is van de opstelling wordt gekarakteriseerd door het meten van het vrije spectrale bereik en de finesse. Een op zichzelf staand hoofdstuk schetst en bespreekt de motivatie van een collineaire laser spectroscopie experiment van ^{42g,m}Sc dat onsuccesvol was, maar zal helpen voor verbeteringen in de toekomst.

Abstract

This thesis presents the development of a saturated absorption spectroscopy setup at the IGISOL facility of the university of Jyväskylä, where the research for this thesis was done in light of an Erasmus exchange of one semester. The goal of this setup in light of high-resolution laser spectroscopy measurements, as well as the underlying theoretical background of this technique and a detailed description of the setup is presented. The dependence on the laser power of the spectra obtained from the saturated absorption spectroscopy of rubidium is studied. The Fabry-Perot interferometer that is part of the setup is characterized by measuring its free spectral range and finesse. A standalone chapter discusses the motivation and outline of a collinear laser spectroscopy experiment on ^{42g,m}Sc that was unsuccessful, but will help to improve future experiments.

Vulgariserende samenvatting

Gedurende lange tijd was het enkel mogelijk om de eigenschappen van stabiele of langlevende elementen te bestuderen, die van nature voorkwamen. Het is daarom niet onlogisch dat de eerste theoretische modellen in de kernfysica er vooral op gericht waren de eigenschappen van deze kernen te verklaren. Dit zijn echter maar ongeveer 254 kernen, terwijl er een paar duizend radioactieve kernen zijn. Al deze onstabiele, kortlevende kernen worden 'exotische' kernen genoemd. Hedendaags onderzoek heeft als doel om na te gaan of de theoretische modellen die gebaseerd zijn op de eigenschappen van (bijna) stabiele kernen in staat zijn om ook de eigenschappen van deze exotische kernen te voorspellen. Om deze vraag te beantwoorden werden faciliteiten gebouwd met het specifieke doel deze exotische kernen te produceren en bestuderen, o.a. de zogenaamde ISOL faciliteiten zoals ISOLDE in CERN, Zwitserland, of IGISOL in Jyväskylä, Finland. ISOL staat voor Isotope Separation On-Line wat de techniek beschrijft om de exotische kernen te produceren. Hoog-energetische deeltjes van een deeltjesversneller worden op een stuk materiaal geschoten. Door de hoge energie vinden kernreacties plaats die allerlei nieuwe isotopen produceren. Uit al deze reactieproducten worden dan isotopen met een bepaalde massa gefilterd die getransporteerd worden naar een experimentele opstelling waar bepaalde eigenschappen kunnen gemeten worden.

Bij veel van deze experimentele opstellingen worden lasers gebruikt. Aangezien experimenten dagen of zelfs weken kunnen duren en een zeer hoge precisie vereisen, is het belangrijk dat alle aspecten van deze lasers zo stabiel mogelijk zijn. In deze thesis wordt de karakterisatie van een opstelling beschreven die gebruikt kan worden bij de stabilisatie van de frequentie van lasers. De opstelling is gebaseerd op gesatureerde absorptie spectroscopie. Deze techniek maakt gebruik van de absorptie van (laser)licht wanneer de gas atomen in een transparante gascel ermee belicht worden. De absorptie zal enkel bij bepaalde frequenties van licht plaatsvinden. Als het licht na de gascel wordt gedetecteerd zal er bij bepaalde frequenties dus een verminderde intensiteit zijn, resonanties genaamd. In sommige configuraties, zoals deze gebruikt in het werk voor deze thesis, zullen deze resonanties scherpe pieken zijn die kunnen gebruikt worden als referentie voor het stabiliseren van de frequentie van een laser. Specifiek in deze thesis is bestudeerd hoe de scherpte van de absorptieresonanties afhangt van het vermogen van het gebruikte laserlicht en zijn de eigenschappen van een belangrijke component van de opstelling gemeten.

Contents

List of Figures

List of Tables

Chapter 1

Introduction and motivation

Since the realization of the first laser in 1960 [11], lasers have found numerous applications in many areas of science, medicine and technology. In physics in particular they are used e.g. in solid state physics to ablate certain layers of materials, in atomic and nuclear physics to trap atoms very precisely and to probe the energy levels of the atom. This master thesis is related to the application of lasers in nuclear physics. One very active research area in nuclear physics is the study of exotic nuclei. These are nuclei far from stability where new phenomena, not observed in stable nuclei, take place. Far from stability however, means that these nuclei are short-lived and must be produced in nuclear reactions. This is possible at dedicated facilities such as IGISOL (Ion Guide Isotope Separation On-Line) at the JYFL accelerator laboratory where exotic nuclei can be studied e.g. by high-resolution laser spectroscopy to measure the hyperfine transitions, in order to deduce information about the nuclear spin, their dipole and quadrupole moments and their charge radius.

To obtain this high resolution, the frequency of the lasers used in the experiments must be very stable with little fluctuations around a chosen preset value, on short term (hours) and long term (days to weeks). Short-term fluctuations are caused for example by acoustic vibrations of mirrors, fluctuations of the discharge in gas lasers or the jet flow in dye lasers. Long-term fluctuations are mainly caused by temperature drifts or slow pressure changes. Various techniques to stabilize the laser frequency exist. Most techniques to stabilize the frequency on long term involve the use of a certain reference frequency with a feedback to the laser. One way to obtain such a reference frequency is with the use of a saturated absorption spectroscopy setup and another very stable laser. In saturated absorption spectroscopy, very sharp resonances can be achieved which are very suitable as a reference frequency if the frequency of the resonances is accurately known. Another way is to use this other very stable laser transmitted through an optical cavity, such as a Fabry-Perot interferometer, as a reference.

The work done for this master thesis is aimed towards testing and characterizing such a saturated absorption spectroscopy setup at IGISOL. This setup may be used to test the long-term frequency stability of a Helium Neon laser and to calibrate home-build Fabry-Perot interferometers. If the Helium Neon laser is stable enough, it will be used as reference to stabilize a continuous wave (cw) titanium-sapphire laser that would be used in high-resolution spectroscopy experiments on exotic nuclei.

Outline

In this first chapter the general framework of the thesis was set. The second chapter will introduce basic concepts and some theoretical foundations of lasers and an introduction to the laser spectroscopy techniques that are important for this thesis, namely saturated absorption spectroscopy and collinear laser spectroscopy. The third chapter gives an overview of the IGISOL facility and the laser spectroscopy setups in particular. In the fourth chapter the obtained data, the analysis of this data and the results from it are presented. The fifth and last chapter is a standalone chapter concerning a collinear laser spectroscopy experiment on ^{42g,m}Sc. Participation in this experiment was part of the work done for this thesis, but as no results were obtained only a motivation and outline are given.

Chapter 2

Introduction to lasers and laser spectroscopy techniques

Lasers have become invaluable tools in various areas of nuclear physics research. They provide intense, coherent and monochromatic light that can be used to probe energy levels of e.g. atoms. This study of the interaction between light and matter is called spectroscopy. It's not possible to directly probe the energy levels of the nucleus because those energies are not yet attainable with lasers. The nuclear structure however influences the atomic levels through an interaction with the electron cloud, called the hyperfine interaction. This gives rise to small splittings in the atomic energy levels, as the degeneracy is lifted, from which information about the nucleus can be derived. The goal of this chapter is to introduce the basic concepts of lasers and laser spectroscopy techniques used in the following chapters.

2.1 Lasers

The term laser originates from an acronym for 'Light Amplification by Stimulated Emission of Radiation'. The basic principle of lasers, stimulated emission, was postulated for the first time by Einstein in 1917 [37]. Stimulated emission is a process by which a beam of radiation passing through a medium can gain energy by inducing excited atoms or molecules (particles) to emit photons identical to those in the beam. This process competes with the inverse process of absorption by which energy is removed from the beam by (re-)exciting particles. In thermal equilibrium the population follows a Boltzmann distribution so there will be more particles in lower energy levels than in excited levels. This means that absorption will always dominate in these cases and energy gain is not possible. To obtain a system where energy gain is possible a population inversion is needed, so more particles should be in excited states than in low-lying states. In the next section an intuitive approach to lasers using the Einstein coefficients will be explained. The section thereafter will discuss the basic design of lasers.

2.1.1 The Einstein treatment

This is a model introduced by Einstein to describe the interaction between matter and light. Although more advanced quantum mechanical models now exist, this model still provides a good introduction due to its simplicity. In this model an atom with two energy

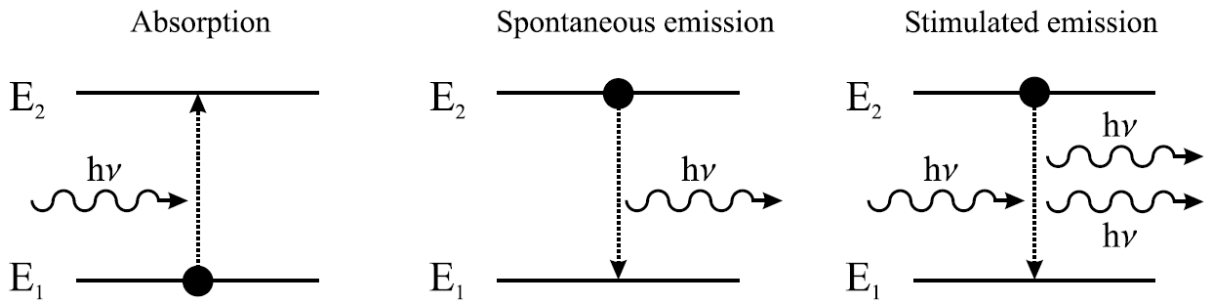

Figure 2.1: The three interactions between a two-level system and a photon postulated in the Einstein treatment [8].

.

levels is considered, an upper level with energy E_2 and a lower level with energy E_1. Radiation can interact with these levels through three processes (fig. 2.7)

1. Spontaneous emission: an atom in the upper level 2 decays to the lower level 1 by emission of a photon with energy $\hbar\nu_{21} = E_2 - E_1$.

2. Absorption: an atom in the lower level 1 is excited to the upper level 2 by the absorption of a photon of energy $\hbar\nu_{21}$.

3. Stimulated emission: an incident photon of energy $\hbar\nu_{21}$ stimulates an atom in the upper level 2 to decay to the lower level 1 by the emission of a second photon of energy $\hbar\nu_{21}$. The stimulated photon is emitted into the same radiation mode as the incident photon. It thus has the same frequency, phase, direction and polarization as the incident photon.

The last process is the key to laser operation. The rates at which this process and the absorption occur must depend on the density of photons of energy $\hbar\nu_{21}$, while the spontaneous process is independent from it.

If an ensemble with $N = N_1 + N_2$ of these two-level atoms is considered in thermal equilibrium with its environment kept at a temperature T, equations for the transitions rates can be postulated. The absorption rate of photons from the environment will be proportional to the transition probability B_{12}, but will also depend on the number of atoms in state $|1\rangle$ and the unknown energy density $u(\nu, T)$ of the radiation field, that depends on the frequency of the radiation ν and the temperature of the system T:

$$\left(\frac{dN_2}{dt}\right)_{abs} = -\left(\frac{dN_1}{dt}\right)_{abs} = B_{12}u(\nu, T)N_1 \tag{2.1}$$

Similarly, stimulated emission causes a transition rate

$$\left(\frac{dN_2}{dt}\right)_{stim} = -\left(\frac{dN_1}{dt}\right)_{stim} = -B_{21}u(\nu, T)N_2 \tag{2.2}$$

Spontaneous emission causes a rate

$$\left(\frac{dN_2}{dt}\right)_{spon} = -\left(\frac{dN_1}{dt}\right)_{spon} = -A_{21}N_2 \tag{2.3}$$

The proportionality constants B_{21}, B_{12} and A_{21} are called Einstein coefficients. They only depend on the properties of the transition and not on those of the radiation field.

From equation 2.3 it can be deduced that in absence of other processes the population of level 2 will decay exponentially with a time constant $\tau_{21} = (A_{21})^{-1}$, called the natural lifetime of level 2. In thermal equilibrium the populations of both levels are constant, meaning

$$\frac{dN_2}{dt} = -\frac{dN_1}{dt} = -B_{21}u(\nu,T)N_2 + B_{12}u(\nu,T)N_1 - A_{21}N_2 \stackrel{!}{=} 0 \tag{2.4}$$

and their ratio can be described by a Boltzman distribution. This leads to

$$\frac{N_2}{N_1} = \frac{B_{12}u(\nu,T)}{A_{21} + B_{21}u(\nu,T)} \stackrel{!}{=} e^{-\frac{E_2-E_1}{k_B T}} \tag{2.5}$$

From this an expression for the energy density $u(\nu, T)$ can be derived. This energy density of the thermal radiation field must follow Planck's law for blackbody (thermal) radiation of temperature T as both must hold for all frequencies and temperatures. Equating both expressions yields

$$u(\nu,T) = \frac{A_{21}/B_{21}}{\frac{B_{12}}{B_{21}}\exp\left(\frac{\hbar\nu_{21}}{k_B T}\right) - 1} \stackrel{!}{=} \frac{\hbar\nu^3}{\pi^2 c^3}\frac{1}{\exp\left(\frac{\hbar\nu}{k_B T}\right) - 1} \tag{2.6}$$

and gives the relations between the Einstein coefficients:

$$\begin{aligned} \frac{A_{21}}{B_{21}} &= \frac{\hbar\nu_{21}^3}{\pi^2 c^3} \\ B_{12} &= B_{21} \end{aligned} \tag{2.7}$$

This result shows that absorption and stimulated emission are completely equivalent processes. Although these relationships were derived under thermal equilibrium, since the coefficients are postulated to be independent of the radiation field they hold in all conditions.

From these equations the requirement of population inversion for optical gain ($N_2 > N_1$) follows from the need for that the rate of stimulated emission must be greater then the rate of absorption. As already stated before, in thermal equilibrium this is impossible. From equation 2.5 it is now obvious that a steady-state inversion is also impossible in a pure two-state system, because

$$\frac{N_2}{N_1} = \frac{B_{12}u(\nu,T)}{A_{21} + B_{12}u(\nu,T)} > 1 \quad \forall u(\nu) > 0 \tag{2.8}$$

is impossible to achieve. The limit is equal populations with infinite pump power ($u(\nu, T) \to \infty$). This is due to the inherent symmetry of the absorption and emission process. In order to solve this problem and to create an inversion, the stimulated emission into the pump wave must be avoided. This is achieved if the stimulated emission towards the lower level occurs at a different wavelength from that of the (pump) absorption. Therefore, at least three levels are needed. The ordering in transitions can be seen in figure 2.2a.

The pump rate is W_p and the laser transition (stimulated emission) is W_{21}. A system is chosen such that the relaxation from level 3 to 2 goes very fast, much faster than the pumping of level 3, so the lifetime of level 3 can be assumed close to zero. Then no

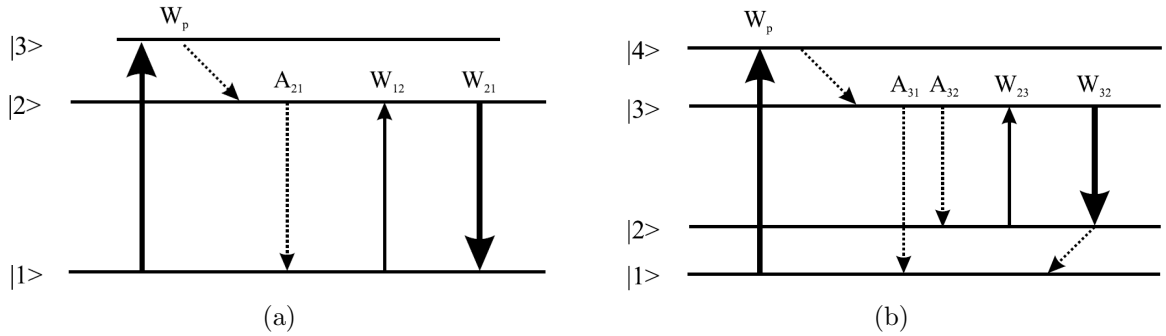

Figure 2.2: Three level and four level system with corresponding transitions [8].

efficient stimulated back-emission into the pump can occur, as the absolute population of level 3 stays nearly zero. The new condition for steady-state inversion is then

$$\frac{N_2}{N_1} = \frac{W_p + W_{21}}{A_{21} + W_{21}} > 1 \text{ for } W_p > \frac{1}{\tau_2} \tag{2.9}$$

where $\tau_2 = A_{21}^{-1}$ is the lifetime of level 2 [8]. This means that the pump rate needs to be stronger for systems with strong spontaneous emission, i.e. for systems with a short second level lifetime.

However, this three-level scheme is still inefficient, as at least 50% of the total population (assuming $N_3 \approx 0$) needs to be pumped into the upper laser level 2 to provide optical gain. Therefore, just to keep the inversion at that level a minimum pump rate of $A_{21}N_2$ is needed. This results in a high laser threshold (the pump power necessary to initiate laser oscillation). To keep this threshold as low as possible, the need for a high upper level population N_2 to reach inversion must be reduced. A similar idea as in going from the two-level to the three-level system can be applied here: reducing the lower laser level population by a relaxation process. This leads to the four level scheme shown in figure 2.2b. A very fast relaxation from level 4 to 3 and from 2 to 1 and a large enough energy separation between 1 and 2 to avoid thermally populating level 2, ensure that the populations of level 4 and 2 are nearly zero. The laser radiation on the transition 3 to 2 thus does not suffer from re-absorption and any population of level 3 causes a population inversion. This four-level laser will therefore show the lowest possible laser threshold.

2.1.2 Design

A laser consists of essentially three components, which can be seen in figure 2.3:

- The active medium, which amplifies an incident electromagnetic (EM) wave;
- The energy pump, which selectively pumps energy into the active medium to populate selected levels and to achieve population inversion as described in the previous section;
- The optical resonator composed, for example, of two opposite mirrors, which stores part of the induced emission that is concentrated within a few resonator modes.

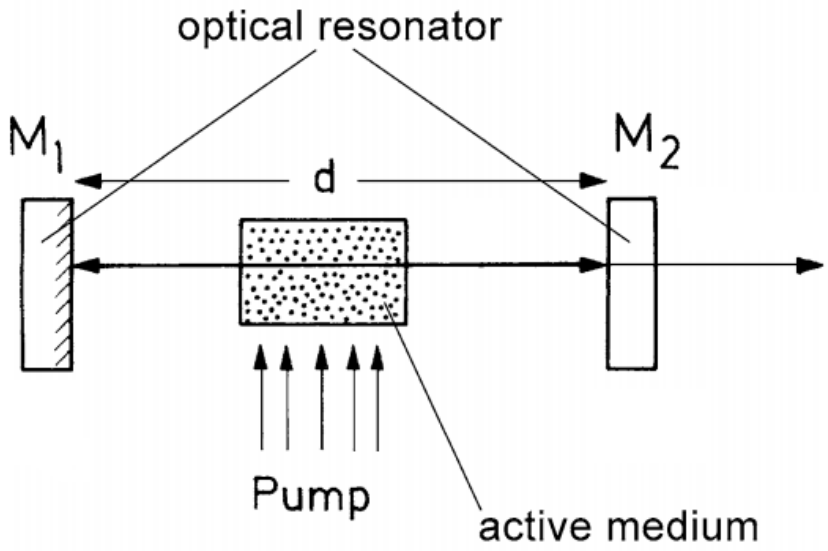

Figure 2.3: Schematic setup of a laser [1].

The condition a laser must fulfill, to ensure that a wave that is reflected back and forth will be amplified despite losses, is the following (derivation in [1]):

$$\Delta N > \frac{\gamma}{2\sigma(\nu)L} \tag{2.10}$$

where ΔN is the inverted population difference, γ the loss coefficient, $\sigma(\nu)$ the frequency dependent absorption cross section and L the length of the active medium. The loss coefficient combines losses from fractional reflection, diffraction by apertures, absorption by the housing of the active medium and scattering.

The function of the optical resonator is the selective feedback of radiation emitted from the excited atoms or molecules of the active medium. As is known from basic optics, in a cavity/resonator the superposition of reflecting waves results in standing waves which only allow certain frequencies to exist. These are called the eigenfrequencies or cavity modes. For a closed cavity (e.g. a box) their number per unit volume in the optical region is given by Planck's distribution $n(\nu)d\nu = 8\pi(\nu^2/c^3)d\nu$ [1]. The number of modes per unit volume within the spectral interval $d\nu$ of a transition turns out to be very large, about 10^5 modes/m^3 in an interval of 1 Hz in the visible range [1]. When a radiation source is placed inside the cavity, its radiation energy will be distributed among all modes and the system will shortly reach thermal equilibrium. Closed cavities with $L \gg \lambda$ are therefore not suitable as laser resonators. To concentrate the radiation energy into a small number of modes in order to enhance stimulated emission into these modes, the resonator should exhibit a strong feedback for these modes but large losses for all other modes.

Such a resonator can be realized with open cavities, which consist of two plane or curved mirrors aligned so that light traveling along the resonator axis may be reflected back and forth between the mirrors. Some rays traverse the active medium many times, resulting in a larger total gain. Rays of other modes inclined against the resonator axis may leave the resonator after a few reflections, before the intensity has reached a noticeable level.

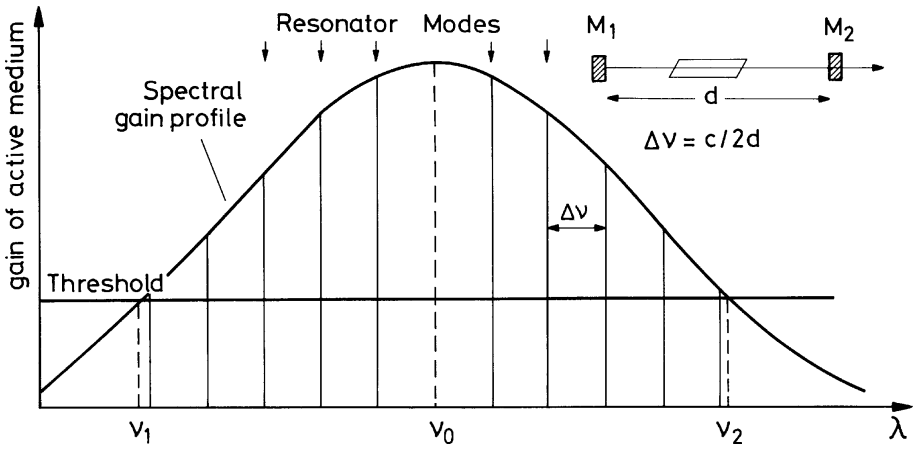

Figure 2.4: Gain profile of a laser transition with resonator eigenfrequencies [1].

Another possible resonator configuration is the ring resonator. A ring resonator consists of at least three reflecting surfaces. Instead of the standing waves in other resonators, the ring resonator allows traveling waves, which may run clockwise or counter-clockwise through the resonator. With an 'optical diode' inside the resonator one direction can be enforced. Such an 'optical diode' is a device that has low losses for light passing in one direction but high losses for light traveling into the opposite direction [9].

The active medium can be any material that fulfills the conditions set in the previous section, especially the conditions for the level scheme. The most common ones are solid-state crystals, semiconductors, atomic or molecular gases and organic dyes. More information on all these types of lasers can be found in [10]. Usually the medium does not have sharp levels as seen in the schemes (fig. 2.2), but rather energy bands. The frequency spectrum of a laser, seen in figure 2.4 is then determined by the gain profile of the laser medium. The spacing between the cavity modes is determined by the cavity length d.

The advantage of lasers with a broad emission spectrum containing multiple modes is that a single laser can be used over a wide frequency range. To obtain again a single-mode beam, additional components are sometimes needed to tune the frequency. When the modes are widely separated, special mirrors with selective reflectivity can be enough. Otherwise prisms, gratings, birefringent filters and/or etalons/Fabry-Perot interferometers must be used.

A birefringent filter (also called Lyot filter) in its most simple form consists of one birefringent crystal plate. The birefringence leads to wavelength-dependent polarization changes and thus transmission losses, arising from the polarization dependence of the reflection at the mirrors and possibly also of the optical gain in the laser medium. The spectral position of the loss minima, where laser operation can take place, can be tuned by rotating the plate. To obtain an optimal transmission spectrum multiple birefringent plates with different thickness separated by air can be used.

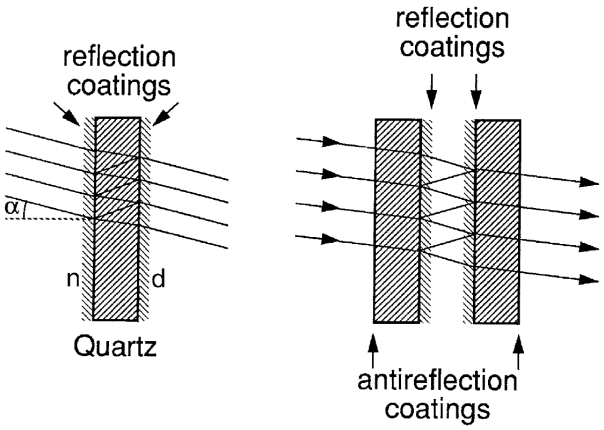

Figure 2.5: Etalon and Fabry-Perot interferometer [1].

2.2 Fabry-Perot interferometer

A Fabry-Perot interferometer (FPI), fig. 2.5, consists of two separate highly reflecting plates, where one surface of each plate is coated with a reflection layer. The two reflecting surfaces are opposed and are aligned to be as parallel as achievable. The outer surfaces are coated with antireflection layers in order to avoid reflections from these surfaces that might overlap the interference pattern. An etalon, fig. 2.5, consists of a plane-parallel glass or fused quartz plate with two coated reflecting surfaces. Both terms are often interchanged, in this section only the term FPI will be used.

The propagation of light through an FPI is shown in fig. 2.6. The multiple reflections of light between the two reflecting surfaces will have constructive or destructive interference, depending on the phase accumulated during propagation, as can be seen in fig. 2.6. A plane wave $E = A_0 \exp[i(\omega t - kx)]$ is incident at the angle θ_i on a plane transparent plate with two parallel, partially reflecting surfaces. The two surfaces have equal reflectivity R and no absorption losses. Two successively reflected partial waves E_i and E_{i+1} have the optical path difference

$$\Delta l = (2nd/\cos\theta_r) - 2d\tan\theta_r \sin\theta_i \tag{2.11}$$

Because $\sin\theta_i = n\sin\theta_r$ (Snell's law), this can be reduced to

$$\Delta l = 2nd\cos\theta_r = 2nd\sqrt{1-\sin^2\theta_r} \tag{2.12}$$

This path difference causes a corresponding phase shift

$$\phi = 2kd\cos\theta_r \tag{2.13}$$

It can be shown [1] that the amplitude of the m^{th} order transmitted beam can be written as

$$A_m = A_0(1-R)Re^{im\phi} \tag{2.14}$$

with a common phase factor removed and A_0 the incident amplitude. The total amplitude is then the sum of all individual beam amplitudes. This is a geometric series and can be expressed analytically. The total transmission intensity T is then [1]

$$T = T_0\frac{(1-R)^2}{(1-R)^2 + 4R\sin^2\phi/2} = T_0\frac{1}{1+F\sin^2\phi/2} \tag{2.15}$$

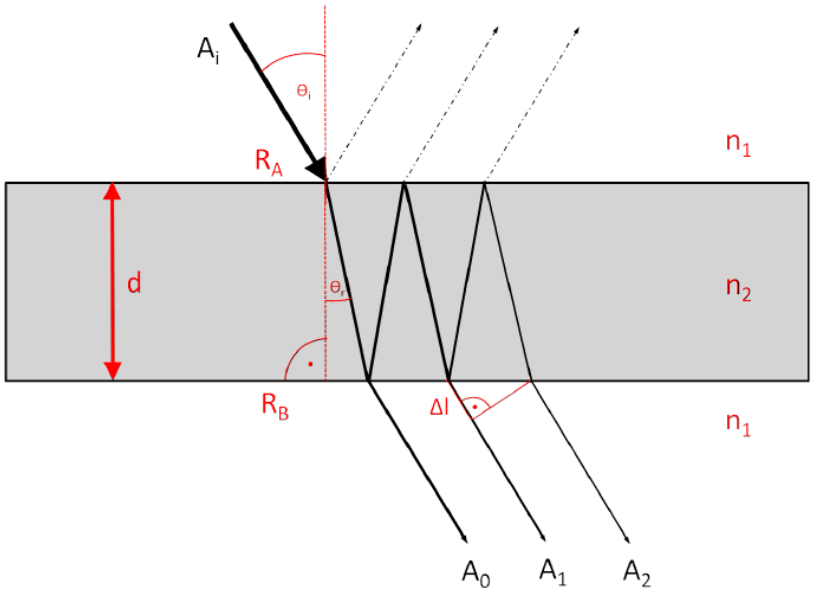

Figure 2.6: Transmission of light through an etalon. Light enters with an angle of incidence θ_i and is partially reflected or transmitted at the surfaces with equal reflectivities RA and RB. Depending on the path taken the beams accumulate a phase delay ϕ. [7].

using the coefficient of finesse $F = 4R/(1-R)^2$. This function is called the Airy function and has a maximum whenever $\phi/2$ is a multiple of π. For normal incidence this happens whenever the optical path length $2nd$ is a multiple of the wavelength λ. In terms of laser frequency ν this means a transmission maximum for every

$$\Delta\nu = FSR = c/2nd \tag{2.16}$$

which is called the Free Spectral Range (FSR) of the FPI. The ratio between the FSR and the full width at hall maximum (FWHM) of the transmission peak is the resolving power of the etalon and is called the Finesse

$$F^* = FSR/FWHM = \frac{\pi}{2\arcsin(\sqrt{1/F})} \approx \frac{\pi\sqrt{F}}{2} \tag{2.17}$$

with the approximation valid for values of $R > 0.5$. Example transmission curves indicating all relevant quantities can be seen in fig. 2.7.

Since an ideal plane-parallel plate, with a perfect surface quality, was assumed, the finesse is determined only by the reflectivity R of the surfaces. In practice, deviations of the surfaces from an ideal plane and slight tilting of the two surfaces cause imperfect superposition of the interfering waves. This results in a decrease and a broadening of the transmission maxima, which decreases the total finesse.

Instead of plane parallel mirrors, it is possible to make a confocal FPI with two spherical mirrors with equal curvatures. A confocal FPI has in general a higher finesse than a plane FPI, as the alignment is less critical and the mirror surfaces can be polished to a higher precision. The finesse will thus be reduced less from the ideal case as described by eq. 4.9. The resolving power will thus be higher, which makes them better suited for applications in high-resolution spectroscopy.

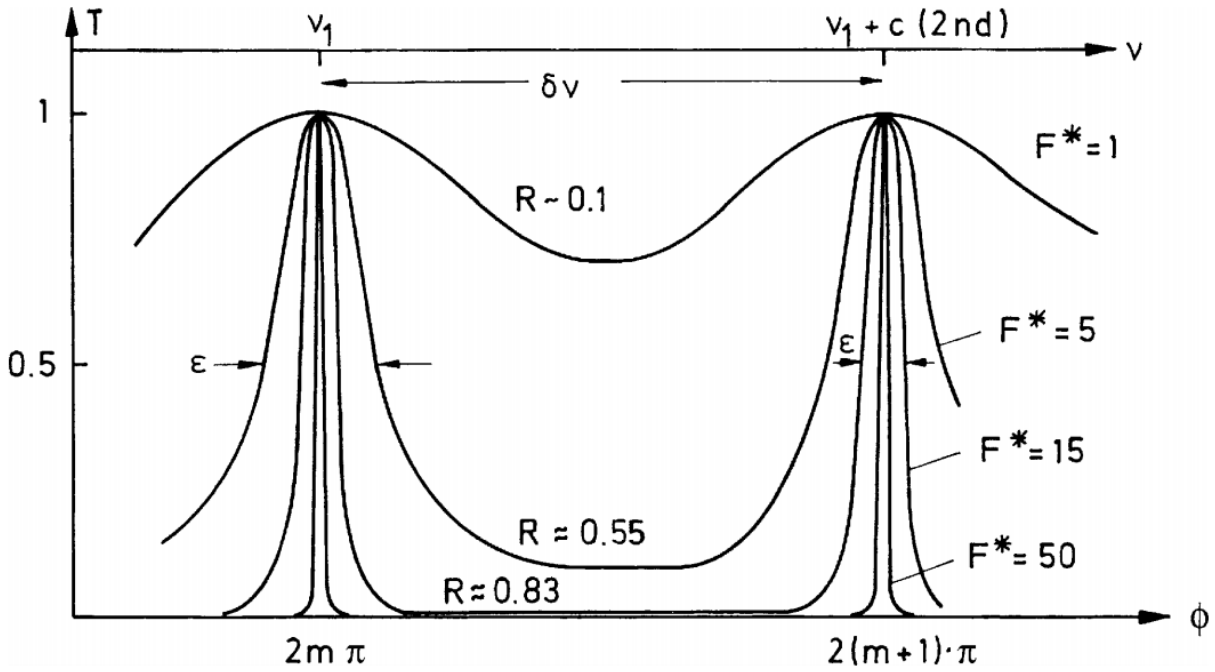

Figure 2.7: Transmittance of an absorption-free multiple-beam interferometer as a function of the phase difference ϕ for different values of the finesse F^* [1].

FPIs are mainly used as wavelength-selective transmission filters within the laser resonator to narrow the laser linewidth. They are also used to investigate the laser mode structure. The accuracy of an FPI is in general better than wavemeters, often based on a Michelson interferometer, which can be affected by various errors [13].

2.3 Structure of atomic spectra

In laser spectroscopy experiments the spectrum of a certain isotope can be measured. To interpret these spectra it is important to understand how these spectra are formed. The basis of a spectrum are the electronic transitions (between fine structure levels). These fine structure energies can be calculated from atomic physics, by considering the nucleus as a positive point charge Ze surrounded by a system of electrons. In reality the nucleus is not a point charge but a complex system of protons and neutrons. This will influence the spectral lines by shifting or splitting them by relatively small amounts, on the order of 10-10^3 MHz, forming the hyperfine structure. By measuring these small shifts and splittings, information about the nucleus can be obtained. In this section the effect of the size and mass of the nucleus will first be discussed and then the effect of the nuclear moments.

2.3.1 Isotope shift

The effect of the nuclear mass and size on the atomic fine structure levels can be observed as a small frequency difference in the atomic transition frequencies, ν^A and $\nu^{A'}$, of two isotopes of the same element. This difference is called the isotope shift

$$\delta\nu^{A,A'} = \nu^{A'} - \nu^A \tag{2.18}$$

This shift can be split up in two separate contributions. The finite nuclear mass gives rise to a small nuclear recoil energy which is called the 'mass shift'. The mass shift is further sub-divided into the normal mass shift and the specific mass shift. The normal mass shift can be easily calculated if the masses are known accurately, the specific mass shift is due to correlations between the electron momenta and requires sophisticated calculations.

The second part of the isotope shift is due to the nucleus not being a point charge, but having an extended charge distribution which changes with the addition or removal of neutrons. The electron fine structure energy of electron levels with a wave function that has a non-zero probability inside the nucleus, will be influenced by the exact size and shape of this distribution due to a different spatial overlap in the electronic and nuclear wave function for different isotopes. This change influences the transition frequencies and is called the 'field shift'.

The field shift is propotional to the mean square charge radius of the nucleus. If the mass shift can be calculated and the electronic factors in the field shift can be determined, it is thus possible to calculate the changes in mean square charge radius from the isotope shift.

2.3.2 Hyperfine structure

The interaction of the nuclear moments with the field produced by the atomic electrons is called the hyperfine interaction and is responsible for a splitting of the atomic energy levels. Due to this interaction the nuclear spin **I** couples to the total angular momentum of the electron **J** to produce the new quantum number F with $\mathbf{F} = \mathbf{I} + \mathbf{J}$ and F ranging from $|I - J|$ to $I + J$. Each atomic level J is then split in $2J + 1$ (if $J < I$) or $2I + 1$ (if $I < J$) sublevels characterized by F and the energy shifts for each hyperfine level are given by [2]

$$\Delta E_F = \frac{1}{2}AC + B\frac{\frac{3}{4}C(C+1) - I(I+1)J(J+1)}{2I(2I-1)J(2J-1)} \tag{2.19}$$

$$\text{with } C = F(F+1) - J(J+1) - I(I+1) \tag{2.20}$$

A and B are called the hyperfine parameters and may be written as:

$$A = \frac{\mu_I B_e(0)}{IJ} \tag{2.21}$$

$$B = eQ_s V_{zz}(0) \tag{2.22}$$

The magnetic hyperfine coupling constant A accounts for the interaction between the magnetic dipole moment of the nucleus μ_I and the magnetic field at the center of the nucleus $B_e(0)$ created by the electrons. The electric quadrupole coupling constant B describes the interaction between the spectroscopic electric quadrupole moment of the nucleus Q_s and the electric field gradient $V_{zz}(0)$.

The hyperfine structure is studied by inducing optical transitions between the F states of two fine-structure levels. Not every transition is allowed. For the dominant electric dipole transitions between a state $|JFm_f\rangle$ and $|J'F'm'_f\rangle$ the following rules apply

$$\begin{aligned} \Delta F &= 0, \pm 1 \\ F = 0 &\nrightarrow F' = 0 \end{aligned} \tag{2.23}$$

This presents a straight-forward way to determine the nuclear spin in the case of $I < J$, by counting the amount of resonances when the nuclear spin determines the number of sublevels.

For $I \leq 1/2$ or $J \leq 1/2$ the second term in eq. 2.19 vanishes which means that no information about the spectroscopic quadrupole moment can be obtained in those situations. If $I = 0$ and $J = 0$ the first term vanishes as well and no information about nuclear moments at all can be obtained. The determination of nuclear moments from these parameters can be possible for radioactive isotopes, because the electronic parts of eq. 2.21 and 2.22, namely $B_e(0)$ and $V_{zz}(0)$, can either be calculated for certain electronic configurations or are known from independent measurements of moments and hyperfine structure on the stable isotope(s) of the same element.

The relative intensity distribution of the hyperfine components for a transition from J to J' are given by the Racah coefficients [12]:

$$S_{FF'} = S(F \to F') = \frac{(2F+1)(2F'+1)}{2I+1} \begin{Bmatrix} J' & F' & I \\ F & J & 1 \end{Bmatrix}^2 \tag{2.24}$$

where the last factor is the Wigner 6j symbol. Typically, the total intensity is normalised to one

$$\sum_{F,F'} S_{FF'} = 1 \tag{2.25}$$

2.4 Line-broadening effects

In this section an explanation of different line-broadening effects will be given as this is crucial for spectroscopy experiments. The natural linewidth of a transition is due to Heisenberg's uncertainty principle and is determined by the decay time τ of the excited state:

$$\gamma_0 = \frac{1}{2\pi\tau} \tag{2.26}$$

Describing the decay of an excited electron configuration using the model of a damped harmonic oscillator, it can be shown (see [1]) that the intensity profile is a Lorentzian function as a function of the decay energy, with the natural linewidth as Full Width at Half Maximum (FWHM).

In addition to the natural linewidth of an optical transition the observed linewidth can be broadened due to a variety of mechanisms. The most important ones are pressure broadening, Doppler broadening and power broadening.

2.4.1 Pressure broadening

Pressure broadening is due to collisions between the atoms and a background gas or between the atoms themselves. There are two kinds of collisions: elastic and inelastic ones. Elastic collisions lead to a positive energy shift of the excited state if the interaction is repulsive and to a negative shift if the interaction is attractive, because of the influence of the interaction potential on the energy levels. These elastic collisions thus lead to a shift of the transition energy, but do not cause broadening. The broadening comes from inelastic collisions, in which the excitation energy of an atom is either partly or completely transferred into internal energy of its collision partner or into translational energy of

both. These collisions lead to an additional depopulation of the excited state besides the relaxation via spontaneous emission. As those collisions are pressure-dependent, the transition probability, and therefore the linewidth, will also be pressure-dependent

$$\gamma = \gamma_0 + \gamma_{press} = \gamma_0 + a p_B \tag{2.27}$$

with the pressure p_B and $a = 2\sigma_{ik}\sqrt{2/\pi\mu k_B T}$ where σ_{ik} is the scattering cross section and μ is the reduced mass of the gas atoms. It can be shown that pressure broadening leads again to a Lorentzian profile but with a broadened linewidth compared to the natural linewidth, given by eq. 2.27 [1].

2.4.2 Power broadening

Power or saturation broadening is due to laser intensities higher than the saturation intensity of the transition. This effect can be illustrated by a two-level system as used previously in section 2.1.1. Referencing to eq. 2.4 the steady-state equations look like

$$\frac{dN_1}{dt} = -\frac{dN_2}{dt} = -B_{12}u(\nu,T)N_1 - R_1 N_1 + B_{12}u(\nu,T)N_2 + R_2 N_2 \stackrel{!}{=} 0 \tag{2.28}$$

where relaxation coefficients $R_{1,2}$ are used instead of the Einstein coefficient A_{21} to allow the inclusion of the relaxation of the lower level. With $N = N_1 + N_2$ and the abbreviation $P = B_{12}u(\nu,T)$ expressions for the population densities of both levels can be obtained

$$(P + R_1)N_1 = (P + R_2)(N - N_1) \rightarrow N_1 = N\frac{P + R_2}{2P + R_1 + R_2} \tag{2.29}$$

and

$$(P + R_2)N_2 = (P + R_1)(N - N_2) \rightarrow N_2 = N\frac{P + R_1}{2P + R_1 + R_2} \tag{2.30}$$

Without radiation field ($P = 0$), the population densities in thermal equilibrium can be expressed as

$$N_{10} = \frac{R_2}{R_1 + R_2}N; \quad N_{20} = \frac{R_1}{R_1 + R_2}N \tag{2.31}$$

An expression for the difference between the population densities $\Delta N = N_1 - N_2$ in general conditions can be deduced:

$$\Delta N = \frac{\Delta N_0}{1 + 2P/(R_1 + R_2)} = \frac{\Delta N_0}{1 + S} \tag{2.32}$$

where $\Delta N_0 = N_{10} - N_{20}$.

The saturation parameter

$$S = \frac{2P}{R_1 + R_2} = \frac{P}{R} = \frac{B_{12}u(\nu,T)}{R} \tag{2.33}$$

represents the ratio of pumping rate P to the average relaxation rate $R = (R_1 + R_2)/2$. If the spontaneous emission of the upper level is the only relaxation mechanism, $R_1 = 0$ and $R_2 = A_{21}$. Since the pump rate arising from a monochromatic wave with intensity $I(\nu)$ is $P = \sigma_{12}(\nu)I(\nu)/\hbar\nu$, the saturation parameter can be written as

$$S = \frac{2\sigma_{12}I(\nu)}{\hbar\nu A_{12}} = \frac{I(\nu)}{I_{sat}} \tag{2.34}$$

where $I(\nu)$ is the intensity distribution and I_{sat} is the saturation intensity of the transition. The saturation intensity for a certain transition can be calculated from the wavelength, transition cross section and upper-state lifetime.

An expression for the power absorbed per unit volume $\frac{dW_{12}}{dt}$ on an atomic transition $|1\rangle \rightarrow |2\rangle$, with the population densities N_1 and N_2, in a radiation field with a broad spectral profile and spectral energy density u can now be obtained using equations 2.32 and 2.33

$$\frac{dW_{12}}{dt} = \hbar\nu B_{12}u(\nu)\Delta N = \hbar\nu B_{12}u(\nu)\frac{\Delta N_0}{1+S} = \hbar\nu R\frac{\Delta N_0}{1+S^{-1}} \tag{2.35}$$

where $B_{12}u(\nu)$ gives the probability to absorb a photon, $\hbar\nu$ is the energy of the photons and ΔN the population difference of the transition.

As already stated before, the unbroadened line profile of an atomic transition is a Lorentzian. The absorption profile $\alpha(\nu)$ of an unbroadened transition will thus also be a Lorentzian. Therefore the induced absorption probability of a monochromatic wave with frequency ν follows a Lorentzian line profile $B_{12}u(\nu) \cdot L(\nu - \nu_0)$. A frequency-dependent spectral saturation parameter S_ν can be introduced

$$S_\nu = \frac{B_{12}u(\nu)}{R}L(\nu-\nu_0) = S_0\frac{(\gamma/2)^2}{(\nu-\nu_0)^2+(\gamma/2)^2} \tag{2.36}$$

where the definition of a Lorentzian function is used and $S_0 = S_\nu(\nu_0)$. Substituting this into eq. 2.35 gives the frequency dependence of the absorbed radiation power

$$\frac{d}{dt}W_{12}(\nu) = \frac{\hbar\nu R\Delta N_0 S_0(\gamma/2)^2}{(\nu-\nu_0)^2+(\gamma/2)^2(1+S_0)} = \frac{C}{(\nu-\nu_0)^2+(\gamma_s/2)^2} \tag{2.37}$$

This a Lorentzian profile with the increased halfwidth

$$\gamma_s = \gamma\sqrt{1+S_0} \tag{2.38}$$

2.4.3 Doppler broadening

The Doppler broadening is related to the Doppler effect where the movement of the atom causes the atom to observe a photon frequency that is modified due to the atoms velocity (related to the temperature). In the non-relativistic approximation the atom sees a frequency given by

$$\nu' = \nu_0\left(1 \pm \frac{v}{c}\right) \tag{2.39}$$

with the positive sign when the atom moves anti-parallel to the photon beam and the minus sign in the opposite case. The thermal motion described by the Maxwell-Boltzmann distribution thus causes a spread of the frequencies observed by the atoms. The probability distribution for the frequencies is

$$P(\nu)d\nu = \sqrt{\frac{mc^2}{2\pi k_b T\nu_0^2}}\exp\left(-\frac{mc^2(\nu-\nu_0)^2}{2k_bT\nu_0^2}\right)d\nu \tag{2.40}$$

This is a Gaussian profile with FWHM

$$\delta\nu_D = \nu\sqrt{\frac{8k_bT\ln 2}{mc^2}} \tag{2.41}$$

Typical values for this Doppler broadening are several GHz at room temperature, which is bigger than the energy splittings in the hyperfine structure.

To summarize, pressure and power broadening result in a Lorentzian profile with linewidths that are typically in the few MHz range, while the Doppler broadening leads to a Gaussian profile with a typical linewidth in the GHz range. Thus high-resolution spectroscopy experiments are only possible in Doppler-free conditions, and that is where collinear laser spectroscopy and saturated absorption spectroscopy play an important role (see further).

When a spectral line experiences all of these broadening effects the resulting profile will be a Voigt profile which is a convolution of a Gaussian and Lorentzian function. In the analysis of spectra the line-broadening mechanisms relevant for the setup must be identified and based on this a suitable profile for the fitting must be chosen.

2.5 Laser spectroscopy techniques

In this section two techniques relevant to this thesis, out of the many laser spectroscopy techniques, will be discussed. Both of these high-resolution techniques are so-called 'Doppler-free' because the achievable linewidth is not limited by Doppler broadening. This is important for the detection of the hyperfine structure because these energy splittings are of the order of μeV, which is very small compared to the few eV separation of the electronic energy levels.

2.5.1 Saturated absorption spectroscopy

Saturated absorption spectroscopy is based on the saturation of inhomogeneous line profiles. Usually these inhomogeneous line profiles are Doppler-broadened transitions. A laser beam is sent through a gaseous sample of molecules with a Maxwell-Boltzmann velocity distribution, leading to a Doppler-broadened absorption profile as described in the previous section. This Doppler-broadening is eliminated by using two counterpropagating beams, called the probe and pump beam, that come from the same laser with frequency ν. For $\nu \neq \nu_0$ photons from the probe beam are absorbed by atoms with the velocity components parallel to the beam

$$v_z = \frac{(\nu - \nu_0)c}{\nu_0} \tag{2.42}$$

where eq. 2.41 was used. Photons from the pump beam are absorbed by other atoms with $v_z = -\frac{(\nu-\nu_0)c}{\nu_0}$. For $\nu = \nu_0$ both beams are absorbed by the same atoms with $v_z = 0$, which essentially move perpendicularly to the laser beams. The intensity per atom absorbed is now twice as large as when $\nu \neq \nu_0$, and the saturation accordingly higher. In other words, some atoms that move perpendicularly to the laser beams will be excited by the pump beam and cannot be excited anymore by the probe beam, leading to a drop in the absorption of the probe beam. This drop is called the Lamb dip.

The absorption coefficient α for this specific case with two counterpropagating beams can be calculated for a gaseous sample in standing wave field [14]

$$\alpha_s(\nu) = \alpha_0(\nu)\left[1 - \frac{S_0}{2}\left(1 + \frac{(\gamma_s/2)^2}{(\nu - \nu_0)^2 + (\gamma_s/2)^2}\right)\right] \tag{2.43}$$

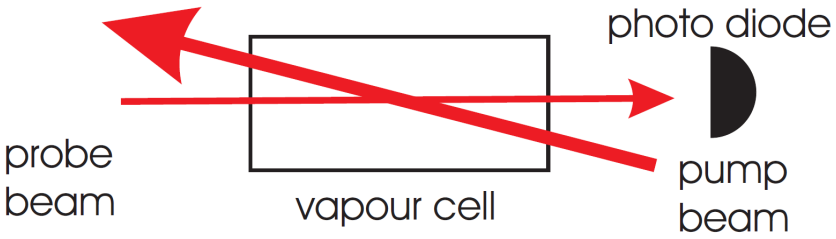

Figure 2.8: Basic experimental arrangement for saturated absorption spectroscopy.

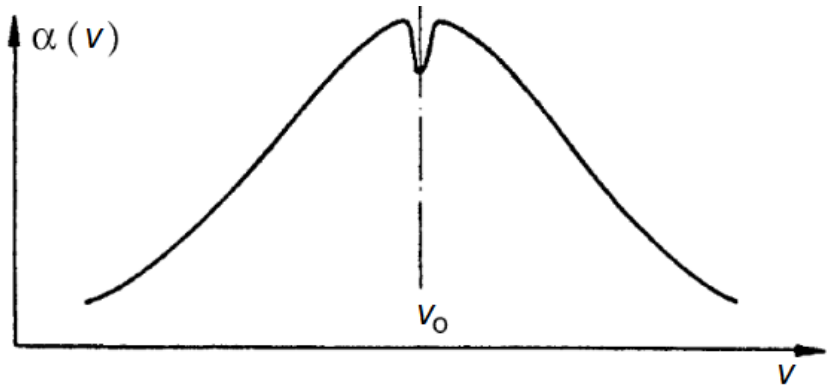

Figure 2.9: Doppler-broadened absorption profile $\alpha_s(\nu)$ with Lamb dip [1].

with $\alpha_0(\nu)$ the absorption coefficient in case of one beam, $S_0 = S_0(I, \nu_0)$ the saturation parameter and γ_s the saturated linewidth given by eq. 2.38. This represents the Doppler-broadened absorption profile with the Lampb dip at the line center $\nu = \nu_0$, where the saturated absorption coefficient drops to $\alpha_s(\nu_0) = \alpha_0(\nu_0) \cdot (1 - S_0)$. The absorption profile is shown in fig. 2.9. The evolution of the absorption profile with the saturation parameter S_0 can be seen in fig. 2.10.

In saturated absorption spectroscopy it is the Lamb dip that will be detected. The spectral resolution is then no longer limited by the Doppler width but by the much narrower width γ_s of the Lamb dip. This is why this technique is considered 'Doppler-free'. To remove fluctuations in overall laser power the laser beam can be split in three instead of two beams. Two of those are again the probe and pump as discussed before and the extra third beam will be the reference beam. The beams are aligned such that the reference beam passes through an unsaturated region of the vapor cell. The signal detected from this beam will this be the normal Doppler-broadened absorption profile. Subtracting it from the signal from the probe beam will then yield the saturation spectrum with only the sharp Lamb dips visible. From these the exact frequencies of the transitions can be determined as the center of the Lamb dip is at the transition frequency ν_0. This technique is thus well-suited to study the hyperfine structure of atoms by sweeping the laser frequency and from this deduce ground-state properties such as nuclear moments.

Besides these Lamb dips there are often other signals in the spectrum as well, called cross-over signals. These occur when two transitions with a common lower or upper level overlap within their Doppler width $\Delta\nu_D$, so $|\nu_1 - \nu_2| < \Delta\nu_D$, as illustrated in figure 2.11. At the laser frequency $\nu_{12} = (\nu_1 + \nu_2)/2$, the pump beam is shifted against ν_1 by

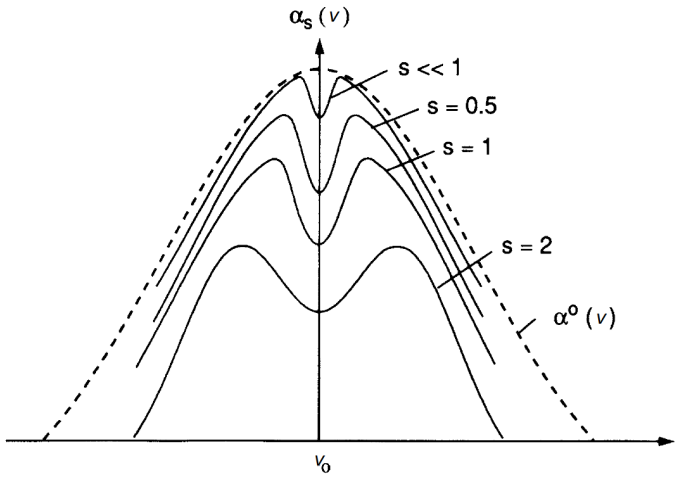

Figure 2.10: Absorption profiles with Lamb dips for several values of the saturation parameter S_0 [1].

$\Delta\nu = \nu_{12} - \nu_1 = (\nu_2 - \nu_1)/2$. It is then resonant with atoms in the subgroup moving with velocity $v_z = (\nu_2 - \nu_1)c/2\nu_{12}$ on transition 1. The counterpropagating probe beam is shifted against ν_2 by $\Delta\nu = \nu - \nu_2 = -(\nu_2 - \nu_1)/2$ and is thus in resonance with atoms in the subgroup $v_z = -(-\nu_2 + \nu_1)c/2\nu_{12}$, as they observe the frequency of the probe beam with opposite Doppler shift. So the same subgroup that is resonant with the pump beam on transition 1, is resonant with the probe beam on transition 2.

Therefore, besides the saturation signals at ν_1 and ν_2 (where the velocity class $v_z = 0$ is saturated), an additional signal (cross-over) is observed at ν_{12}, exactly at the center between the two transitions 1 and 2 where the two Doppler broadened absorption profiles cross (fig. 2.11). In case of a common lower level this is because the pump causes a decrease $-\Delta N_1$ of the population density N_1 in the common lower level, which leads to reduced absorption of the probe beam as for the normal saturation signals.

When the common level is the upper one both beams contribute at at ν_{12} to the increase ΔN_2 of the population N_2, one beam on transition 1, the other on 2. This can lead to enhanced absorption due to optical pumping effects. Optical pumping occurs when atoms in the excited level spontaneously decay to either lower level more or less equally. If the atom is resonant with only one transition, each time it is promoted from the "resonant" lower level to the excited level, some fraction of the time it will decay to the "non-resonant" lower level. Once in the non-resonant lower level, the atom no longer interacts with the laser field. Lower level populations, and thus the amount of absorption, can be significantly altered by optical pumping. When the atom is however resonant on two transitions, at ν_{12}, atoms in both lower levels interact with the laser field. This can possibly enhance the absorption of the probe beam as no atoms are 'lost' to a non-resonant level.

2.5.2 Collinear laser spectroscopy

Collinear laser spectroscopy is a conceptually very simple method of high-resolution laser spectroscopy. A fast ion (or atom) beam is superimposed with a narrow-band laser beam. If the laser frequency is in resonance with an atomic transition, excitation takes place.

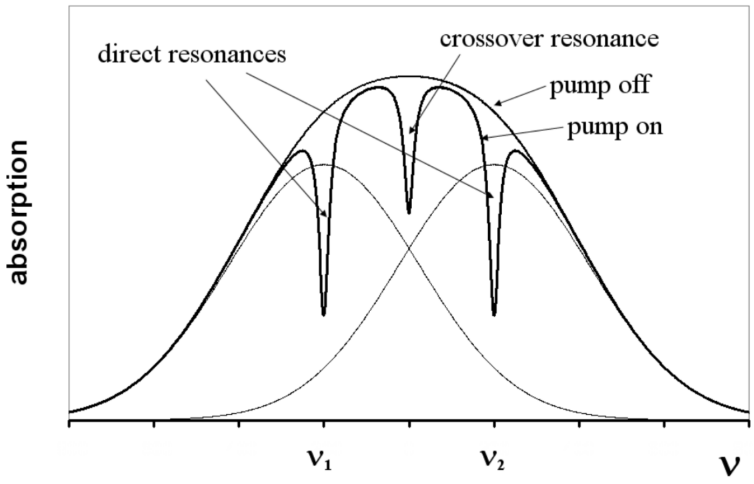

Figure 2.11: Illustration of crossover signals [1].

This can be detected by observing the fluorescence light from the decay back to the original or to a third state. A full spectrum is obtained by sweeping the laser frequency across the resonance(s). This can be achieved by actually tuning the laser itself but in practice, this is difficult to accomplish. High and stable laser intensities are for instance hard to achieve when scanning the laser frequency. Instead, the technique takes advantage of the Doppler effect. In the reference frame of the accelerated ions the laser frequency ν_L is shifted according to

$$\nu_{ion} = \nu_L \sqrt{\frac{1-\beta}{1+\beta}} \tag{2.44}$$

where β is due to relativity

$$\beta = \frac{v}{c} = \sqrt{1 - \left(\frac{mc^2}{eV_{acc} + mc^2}\right)} \tag{2.45}$$

The frequency observed by the ions ν_{ion} can thus be changed by adjusting the acceleration voltage V_{acc} (from electrostatic lenses). This method of effectively scanning the frequency is called Doppler tuning.

The use of accelerated ions also allows to overcome the resolution limits set by the Doppler broadening. When the ions leave the ion source, they have a certain spread on the kinetic energy δE. Upon acceleration by a high voltage $V_{acc,tot}$, all ions experience the same increase in kinetic energy $eV_{acc,tot}$ and the energy spread remains constant. An increase in velocity then results in a reduced velocity spread due to the relation between energy and velocity

$$\delta E = \delta \frac{mv^2}{2} = mv\delta v \tag{2.46}$$

Using $v = \sqrt{2eV_{acc}/m}$ and eq. 2.41 the expression for the Doppler width becomes

$$\delta\nu_D = \nu \frac{\delta E}{\sqrt{2eV_{acc}mc^2}} \tag{2.47}$$

Using typical values of about 1 eV for the original energy spread and a few kV for the acceleration, the Doppler width is reduced to about 10 MHz, comparable to the natural line width.

Chapter 3

Experimental setup

All experiments conducted or participated in for this thesis took place at the IGISOL facility at JYFL, Jyväskylä. This is an Ion-Guide Isotope Separation On-Line facility where pure beams of exotic nuclei can be produced by bombarding targets with beams from particle accelerators. These exotic nuclei can then be used in various experiments. In this chapter the facility will first be discussed in general. The next section will zoom in on the collinear laser spectroscopy setup at one of the beamlines. The last section will discuss the saturated absorption spectroscopy setup used to obtain the experimental data presented in the next chapter.

In 2014 an overview of the research conducted using the IGISOL technique at the JYFL accelerator laboratory was published [25]. This IGISOL Portrait provides a general introduction to the whole facility where more information can be found.

3.1 The IGISOL facility at JYFL

A schematic of the current facility, IGISOL-4, can be seen in figure 3.1. Beams from two cyclotrons, the K130 and MCC30/15, can be directed to the target chamber. The K130 can deliver a large variety of heavy- and light-ion beams up to an energy of $130q^2/A$ MeV, however, most commonly used are protons. The MCC30/15 is an accelerator for protons (18 - 30 MeV) and deuterons (9 - 15 MeV). Additionally there is a spark source to produce stable beams. Well-known stable beams can be used in between on-line experiments to e.g. study systematic effects, test new possibilities for experiments and check and tune the beamlines immediately prior to an on-line experiment.

At IGISOL the ion-guide method is used for the production of exotic nuclei. This technique was pioneered at JYFL and is a variation on the helium-jet technique. The thin-foil target is installed directly in a gas-filled chamber, the ion guide, where it can be bombarded with particle beams from the cyclotron. This gives rise to various nuclear reactions, such as fission, spallation or fragmentation depending on the target and the beam. The exotic nuclei produced in these reactions are called the reaction products. These are transported from the chamber in a fast-flowing gas-jet. The ion-guide technique has a short extraction time, which provides the opportunity for very fast mass separation. This is the main advantage of the ion-guide method compared to the hot-cavity method, where the extraction takes more time as products have to diffuse out of the thick target. Besides that the technique is independent of the recoil volatility. This is another advantage compared to the hot cavity ion sources where isotopes of refractory elements cannot (or

very poorly) be extracted [26]. Different ion guides have been developed throughout the years. At the moment light-ion guides, for light-ion fusion-evaporation reactions, and ion guides for fission reactions are available. An ion guide for heavy ion reactions has been commissioned. Laser access to the ion-guide is possible to make the technique element-selective by resonant ionization. The reaction products are partially neutralized by collisions with the buffer gas inside the ion guide. A certain element is then resonantly ionized upon exiting the ion guide. This has been tested already on e.g. Yttrium [28].

After extraction from the nozzle of the ion guide the products are focused using a radiofrequency (RF) multipole device, namely a sextupole-ion-beam guide (SPIG). This consists of six rods, equally spaced on a circle in a plane perpendicular to the axis of symmetry, on which a RF electric field is applied. The SPIG replaced the original skimmer and improved the ion transports by a factor of typically 4 to 8 [27]. Laser access to the SPIG is provided as well since there are plans to do resonant ionization inside the SPIG in light of the Laser Ion Source Trap (LIST) project [29, 30]. For this reason there is also a repeller electrode at the entrance that can be put to a positive potential to prevent any non-neutral fraction from entering the SPIG, ensuring that all ions that are extracted are resonantly ionized ions. A final end electrode is used to optimize the ion transport through the SPIG.

The reaction products are then accelerated to 30 keV and mass separated using a dipole magnet, with a typical mass resolving power of about 1:500 [15]. From the switchyard after mass separation the beam can be directed to the RFQ cooler-buncher, to a spectroscopy line or in the future to possible other setups. The RFQ cooler-buncher is a gas-filled Paul trap. The ions are cooled down due to collisions with the gas and 4 quadrupole rods with an applied RF field provide the trapping potential. Bunches can be made by only releasing the ions during a certain short time. The typical holding time is about 100 ms resulting in a 10 to 15 μs bunch, but the holding time can vary depending on the half-life of the isotope under study. After the cooler-buncher the beam can be directed to the JYFLTRAP double Penning trap [35] or to the collinear laser beam line by using quadrupole bends. Direct access for lasers to the cooler-buncher and the target chamber is provided.

3.2 Use of lasers at IGISOL

Various lasers are in use at IGISOL for different kinds of experiments. The main project with lasers is the Fast Universal Resonant laser IOn Source (FURIOS). This is an all solid-state laser system that can be used for (resonance) laser ionization or optical pumping with an almost universal coverage of the periodic table. It consists of five pulsed Ti:Sa broadband lasers pumped by two Nd:Yag lasers. Three "standard" Ti:Sa lasers are used for on-line experiments. A grating-based Ti:Sa laser is used for development of new ionization schemes. The fifth laser, an injection locked Ti:Sa laser, has been developed for high-resolution spectroscopy in the gas jet. The three standard lasers are all equipped with etalons and birefringent filters to tune the frequency. The fundamental light of Ti:Sa lasers is in the infrared, but with the use of nonlinear crystals the frequency can be doubled, tripled or quadrupled. This process is called Second/Third Harmonic Generation (SHG/THG). Photons interact when passing through such a nonlinear crystal and generate photons with twice the energy and thus half the frequency of the original photons.

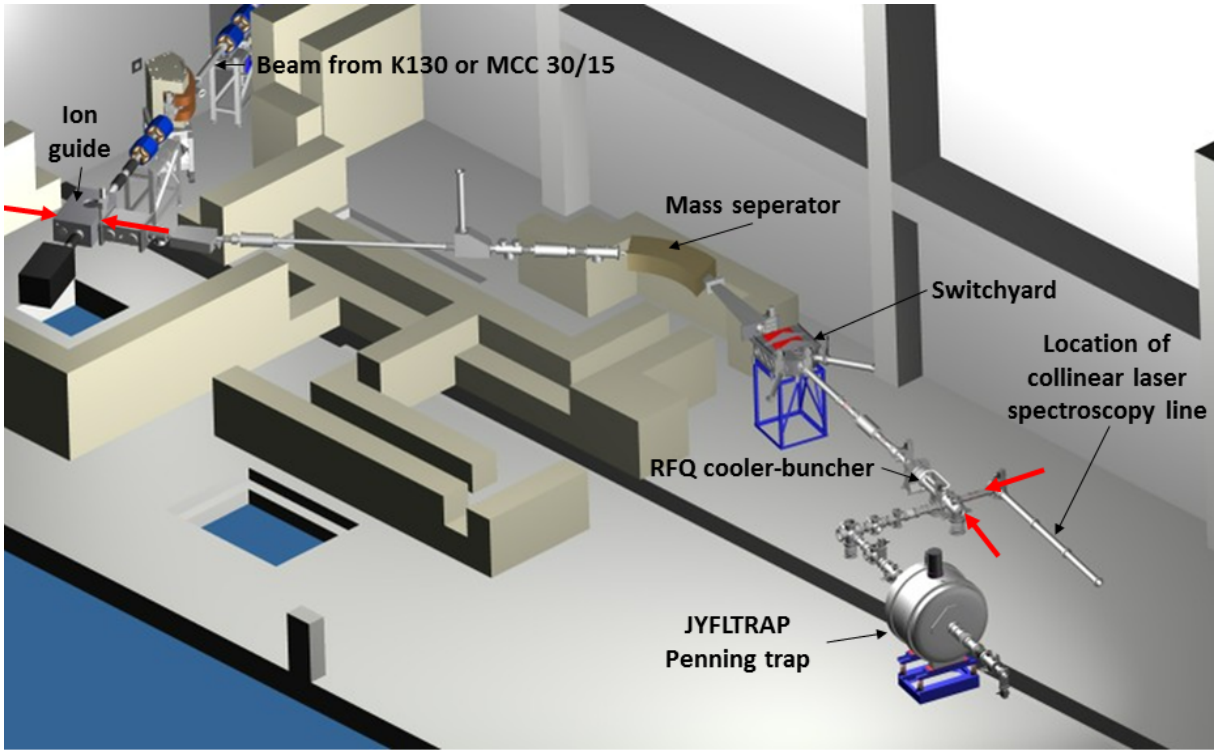

Figure 3.1: Layout of the new IGISOL-4 laboratory. The red arrows indicate typical laser access possibilities.

Doubling crystals (SHG) can be put inside the laser cavity or outside, higher orders must be generated outside the cavity. The benefit of putting doubling crystals inside the cavity is the fact that the light then passes through multiple times generating more power in the frequency doubled light, but it is more difficult to setup due to phase-matching and other requirements. In general the crystals are put inside the cavity if the laser power is too low to achieve the necessary power in the second harmonic. The lasers from FURIOS are used for resonance ionization as described in the previous section for optical pumping in the RFQ sometimes needed in collinear laser spectroscopy experiments, e.g. [32]. There is also an Atomic Beam Unit (ABU) providing beams of stable elements to continue to develop the laser systems for future plans such as in-source and in-jet spectroscopy.

Besides the five pulsed Ti:Sa lasers from FURIOS there is also a continuous wave (cw) Ti:Sa laser (Sirah Matisse TS). The optical design of this laser can be seen in figure 3.2. All components are discussed in section 2.1.2. The selection of a single frequency mode of the laser is done by stepwise scanning the birefringent filter, the thin etalon and the thick etalon. In figure 3.3 this stepwise selection is shown. The first selection out of the full intrinsic emission spectrum is already done by the mirrors (e.g. MOS-2) as they only reflect light in a certain wavelenght range. The birefringent filter is the main broad-range tunable element. To achieve a single frequency two etalons are then needed. A solid state etalon (called Thin Etalon) is used to further narrow the range, and a piezo-driven Fabry-Perot interferometer (called Thick Etalon) to select a single mode. For both etalons one of their mode's frequency has to be the same as the laser resonator mode's frequency. To ensure this both have a control loop that changes the position (Thin) or the spacing

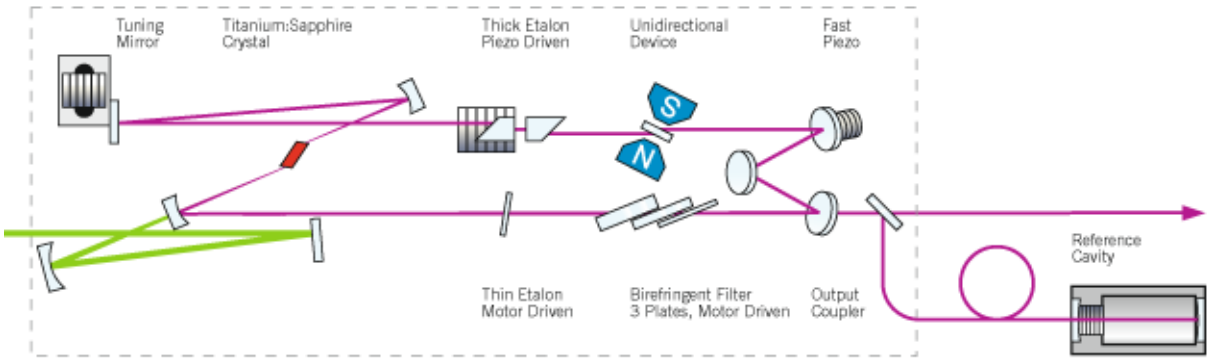

Figure 3.2: Optical design of the Sirah Matisse TS cw Ti:Sa laser [18].

between the prisms (Thick) when needed. The frequency of the laser can be scanned by adjusting the cavity length with the piezo driven tuning mirror. Short-term frequency stability is controlled by the external fiber-coupled reference cavity and a feedback loop to the fast piezo. This laser is currently not directly used for on-line experiments, but as a seed laser for an injection-locked Ti:Sa laser [7]. There are plans to use this laser for collinear laser spectroscopy experiments in the future.

Further also a cw dye Spectra Physics 380 laser is used for the collinear laser experiments. By changing the dye a wide range of frequencies can be accessed. The frequency is tuned with etalons, a birefringent filter and dual galvoplates. Frequency doubling is also possible by introducing a crystal in the cavity. The frequency can be chosen and locked to a reference transition of an iodine absorption cell [1].

3.3 Collinear laser spectroscopy at JYFL

The collinear laser spectroscopy setup at JYFL is managed by the universities of Jyväksylä, Birmingham, Liverpool and Manchester. A schematic of the setup can be seen in figure 3.4. The spectra are recorded with optical detection using one photomultiplier tube (PMT). Thanks to the fast extraction and the chemical insensitivity of the IGISOL technique already mentioned before, a lot of refractory and short-lived isotopes can be studied at JYFL that cannot be studied at hot cavity ion source facilities. The cooler-buncher reduces the spread in energy, providing better resolution, and the spatial spread, providing better overlap with laser beams. Such a cooler-buncher was first developed at JYFL [31]. A reduction in background is obtained using the photon-ion coincidence technique, where as the name says coincidence between bunches and photons is demanded. This method was pioneered at Jyväskylä [38, 31]. In the interaction region the beam is carefully overlapped with the counter-propagating laser beam. The laser used is the cw dye laser discussed in the previous section.

There are plans to install a charge exchange cell (CEC) before the interaction region. A CEC is a gas cell filled with hot alkaline vapor and is used to neutralize ions by the following reaction:

$$A^+ + X \rightarrow A + X^+ + (\Delta E \approx 0) \tag{3.1}$$

where A is the element under study and X is the selected gas. The gas is selected based

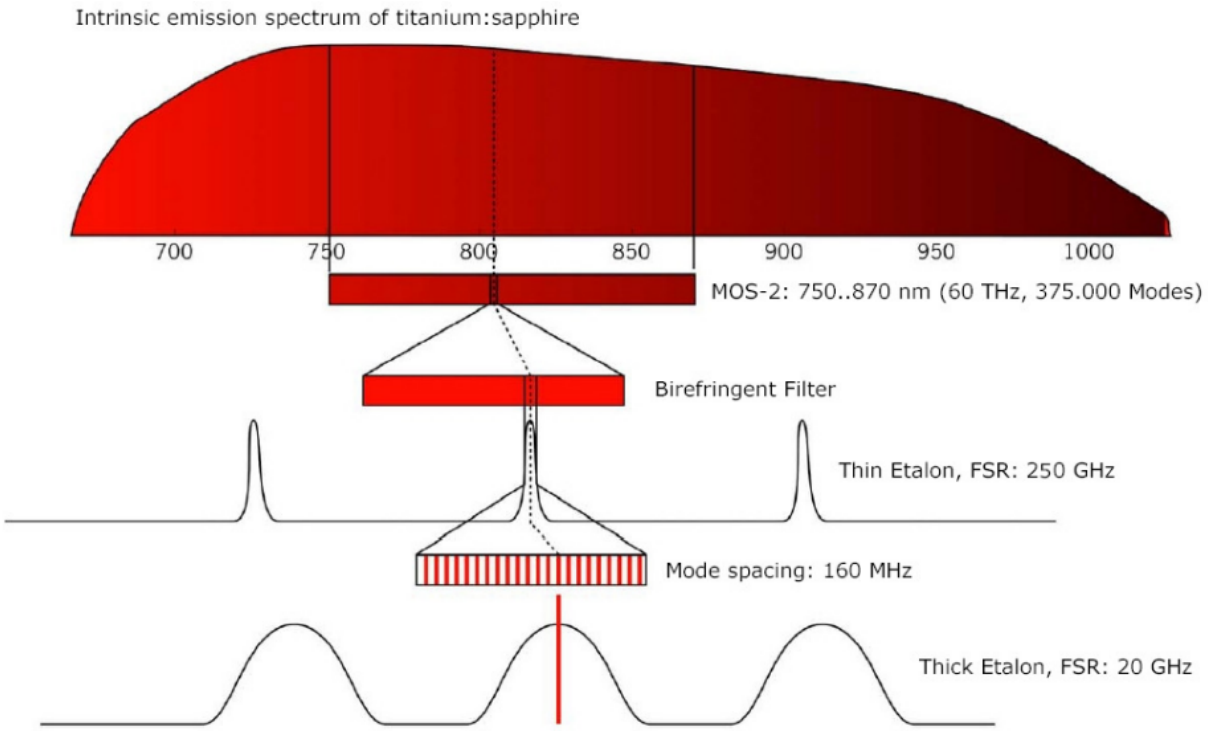

Figure 3.3: Single mode selection in the Matisse cw Ti:Sa laser.

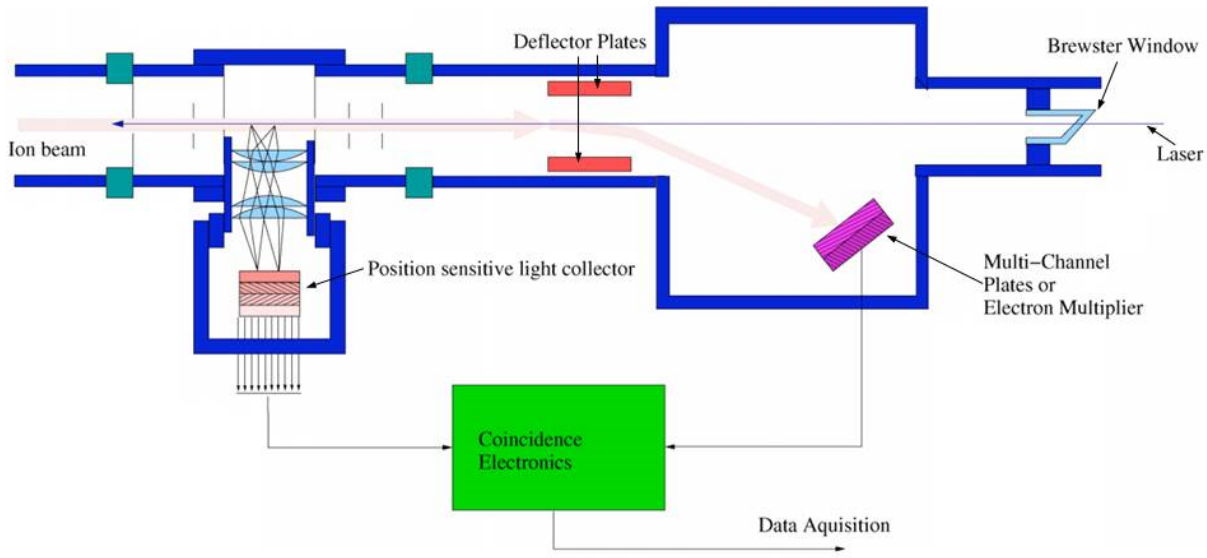

Figure 3.4: Schematic of the collinear laser spectroscopy beamline at IGISOL.

on the requirement to have $\Delta E \approx 0$ to make the reaction as effective as possible. The neutralization of elements is sometimes needed when the transitions in the ion cannot be accessed by the dye laser. Neutral atoms often have transitions in the infrared where a Ti:Sa laser would be well suited for. Another technique that would be possible after the installation of a CEC is resonant ionization. Instead of just exciting the atoms with the laser light they are then ionized in multiple steps. Ion detection is much more efficient than photon detection leading to an overall better sensitivity. First tests have already been conducted [16]. Recently an experiment dedicated to this technique called CRIS was installed at ISOLDE, CERN [34].

The focus throughout the years has been on certain areas of study. These are the sudden onset of deformation at $N = 60$ [32], multi-quasi particle isomers [33] and the $Z = 20 - 28$ calcium and nickel region [4]. In reference [3] a detailed table with all measured isotopes and isomers can be found. Most of these areas remain a priority for new measurements. New possible areas include the refractory regions around nickel ($Z = 28$), ruthenium ($Z = 44$) and rhenium ($Z = 75$). The new fission ion guide will also allow studies of very neutron-rich nuclei.

3.4 Saturated absorption spectroscopy setup

Saturated absorption spectroscopy on an element with a very well-known hyperfine structure is often used to provide very precise frequency benchmarks. These benchmarks can be used among others to calibrate Fabry-Perot interferometers or to check the stability of the laser frequency over long periods of time. These are also the main reasons a saturated absorption spectroscopy setup using a rubidium-filled gas cell (Thorlabs, GC25075-RB) was built at IGISOL. The setup can be see in figure 3.5. The gas cell is filled with natural rubidium, meaning the isotopes ^{87}Rb (72.168%) and ^{85}Rb (27.835 %). The D1 transition at $\lambda = 794.978$ nm [5, 6] is used because it is well suited to the fundamental light of the used laser, the narrow linewidth cw Ti:Sa laser already described in section 3.2. More information on the isotopes and D1 line can be found in [5, 6].

The main Ti:Sa laser is located in another cabin and thus coupled in through a polarisation maintaining, single mode, optical fiber. The beam first passes through a waveplate ($\lambda/2$) and a polarizing beamsplitter (PBS) cube. The waveplate transforms the horizontally polarized light into a linear combination of horizontal (p-) and perpendicular (s-) polarized light. The PBS cube then transmits the p-polarisation and reflects the s-polarisation contribution. The purpose of this is to have two beams of variable ratio, here one goes to the saturated absorption setup and the other to the injection-locked laser. After a pick-off mirror, part of the laser beam is split in two by reflecting it on the front and back end of a thick glass plate. One of these beams is the reference beam and the second one the probe beam as described in section 2.5.1. Both of these beams have a diameter of about 1 mm. They are recorded by two individual photodiodes (Thorlabs, FDS100). The laser beam that passes through the glass plate is expanded to a larger diameter of about 3 mm using a telescope and then overlapped with the probe beam by reflection of a D-shaped mirror. This larger sized beam is the pump beam. To prevent reflections of the pump beam off the windows of the gas cell to enter the photodiodes the gas cell is slightly tilted. To change the power of the pump beam a manual filter wheel was introduced right after the telescope. The wheel is mounted with several different neutral density filters,

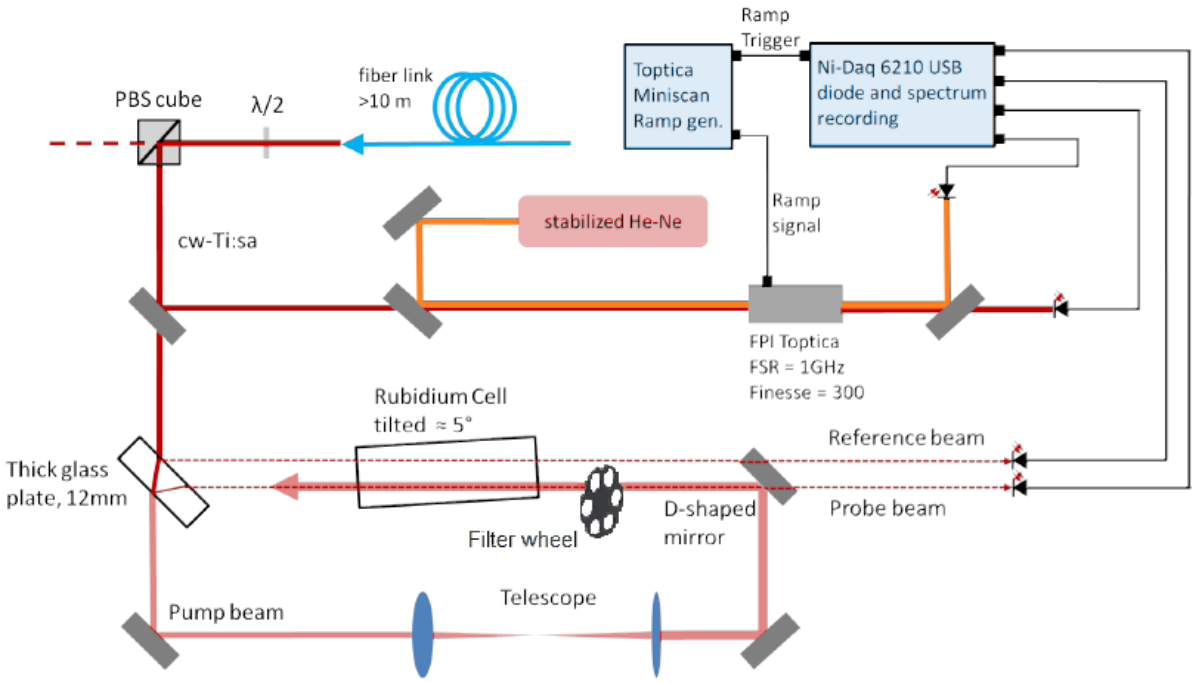

Figure 3.5: Saturated absorption spectroscopy setup for rubidium [7].

which have an almost constant degree of attenuation in a substantial wavelength range.

Besides the main setup part of the Ti:Sa beam also goes to a scanning Fabry-Perot interferometer (Toptica FPI-100-0750-y) together with a frequency-stabilized HeNe laser beam with wavelength 632 nm. The basics of an FPI were already described in section 2.2. According to the technical specifications, the FSR of this FPI is 1 GHz and the finesse is at least 400 [20]. A scanning FPI however has one movable mirror. The frequency-dependent location of the transmission peaks makes a scanning FPI an excellent tool to measure changes in frequency, e.g. while scanning a laser. The accuracy of the frequency determination will depend on the finesse of the FPI. The FSR in this case determines the wavelength interval $\delta\lambda$ of the laser light for which a one-valued relation exists between the wavelength λ and the position of the transmission peaks. This means that the FPI can only determine λ modulo $\delta\lambda$ so when scanning over a wider range the frequency can only be set using a chosen known reference from e.g. a wavemeter or a certain atomic transition. The transmission frequencies in a scanning FPI are tuned by adjusting the length of the cavity using piezoelectric transducers. A trigger from the FPI ramp generator starts a new scan and sends a signal to the data acquisition system, called the ramp signal. This results in a spectrum where the peaks between two ramp signals are due to constructive interference related to the position of the mirror. In this setup two laser beams are sent through the FPI, one with constant frequency (HeNe) and one with changing frequency (Ti:Sa).

To obtain a clear and well resolved spectrum it is important that both laser beams are mode-matched to the resonator cavity. This is done by adjusting the mirrors that determine how the beams enter the FPI. After entering the FPI, a dichroic mirror separates the two beams as a dichroic mirror reflects certain wavelengths and absorbs others. This separation is not perfect however, so some light from the HeNe is transmitted and

recorded by the Ti:Sa photodiode. The frequency of the Ti:Sa can be determined from the change in its peak positions relative to the fixed peaks from the HeNe. The exact procedure will be explained in the next chapter when discussing data analysis.

The signals from the two photodiodes after the Rb cell, the two photodiodes in the FPI and the ramp signal are inputs for the data acquisition system. The data acquisition system from National Instruments (NI USB-6210) has a sampling rate of 250 000 samples per second. It has 16 analogue voltage input channels, but the sampling bandwidth is shared between all channels that are being used. In this case, with 5 channels, it means that the maximal sampling frequency of each channel is 50 kHz. The data is then saved and displayed with a simple program made in Labview.

Improvements to the setup

During the work for this thesis, some problems with the setup were discovered. The first problem was large fluctuations in the overall power output of the fiber. This was due to a damaged optical fiber which was then replaced. Replacing a single mode optical fiber must be done carefully as good input coupling is crucial. Single-mode fibers are designed to only support a single propagation mode per polarization direction, the transverse mode, for a given wavelength. The advantage is that the transverse intensity profile at the fiber output has a fixed shape, which is independent of the launch conditions and the spatial properties of the injected light. The launch conditions only influence the efficiency with which light can be coupled into the guided mode. To maximize the efficiency the light must have a focus at the fiber's input and the beam profile must have the correct size and shape and be precisely aligned.

The second problem was again related to power fluctuations. It was noticed that there was a parabolic fluctuation in the difference between the two photodiode signals as can be seen in figure 3.6. This fluctuation is perfectly symmetric while scanning the frequency of the Ti:Sa up and down. This is related to the fact that the two photo diodes are not perfectly balanced and thus don't record changes in the overall power to the same extent. The cause of the periodic change in the power was discovered to be the slight steering of the Ti:Sa laser while scanning the frequency. This steering influenced the fiber input coupling which resulted in a change in output power. A solution to this is to defocus the laser beam a bit at the input so the overlap between the focus spot and the fiber core is preserved while scanning. This reduces the output power of the fiber but ensures that it is stable. The solution however was only found after the data for this thesis was already recorded so in the data analysis the 'parabolic background' of the spectrum needs to be taken into account.

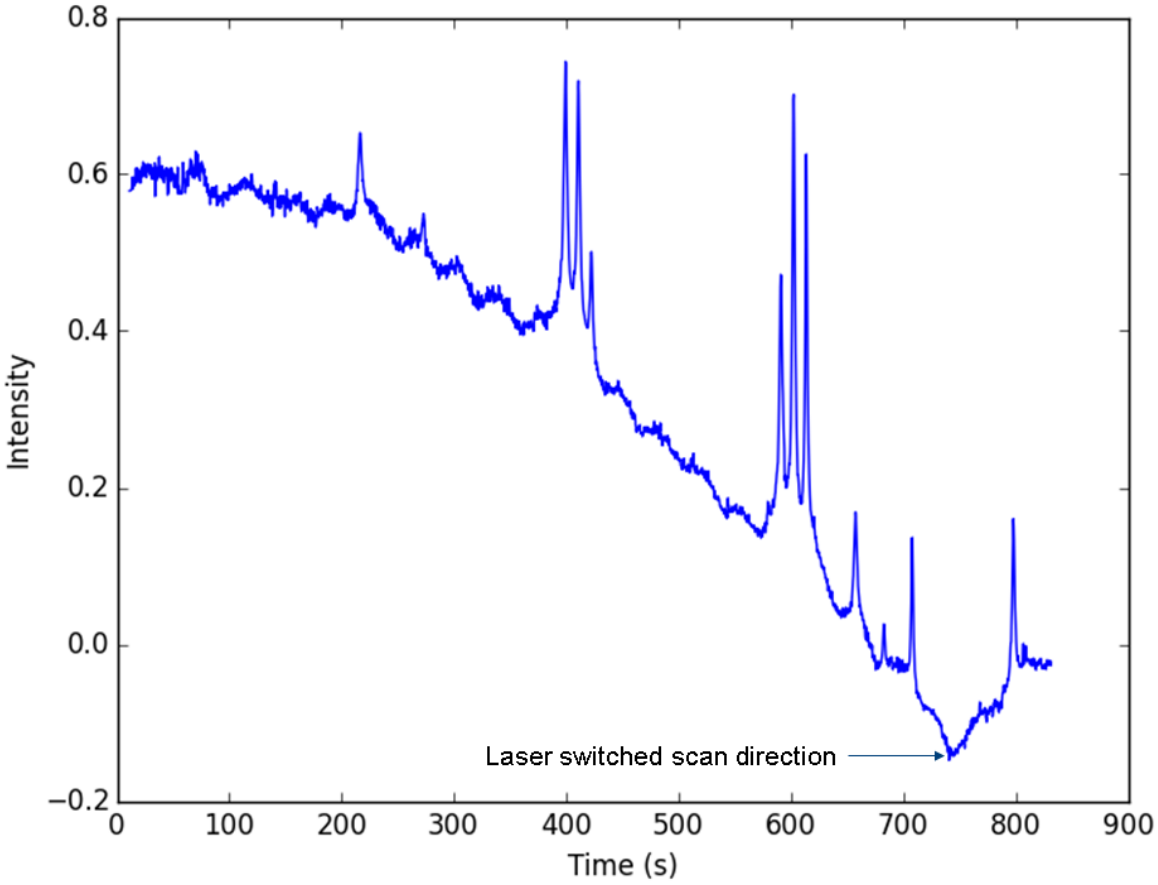

Figure 3.6: Difference signal between the two photodiodes. The parabolic fluctuation is clearly visible.

Chapter 4

Results and analysis

In this chapter the data collected from the saturated absorption spectroscopy setup, the analysis and results of those data will be presented. This consists of investigating the power dependence of the saturation spectra and the characterization of the FPI in the setup. All the analysis was done in Python 2.7.

4.1 Data collection and handling

As stated before, the signals from the two photodiodes after the absorption cell, from the two photodiodes after the FPI and the trigger signal of the ramp generator are recorded by using Labview. In total eight spectra were recorded, each with a different pump beam power by using the filter wheel after the telescope. As these data files were all about the size of 1 GB they were first split up in separate files, one containing the absorption signals and one containing the FPI signals. The absorption signals from the probe and reference beam were averaged by calculating the average of data points in a certain interval, with the standard error on the mean as error on each data point. The signal from the reference beam was then subtracted from the signal from the probe beam to obtain the saturation spectrum. The error on the difference was calculated using the well-known formula for error propagation with correlated errors for a function $f(a, b)$

$$\sigma_f^2 = \left(\frac{\partial f}{\partial a}\right)^2 \sigma_a + \left(\frac{\partial f}{\partial b}\right)^2 \sigma_b + 2\frac{\partial f}{\partial a}\frac{\partial f}{\partial b}\sigma_{ab} \tag{4.1}$$

where σ_i are the standard errors and σ_{ab} is the covariance. The FPI signals are not averaged as that would average out the closely spaced transmission peaks but just saved in a separate file.

4.2 Conversion to frequency

To be able to analyze the saturation spectra a conversion of the recorded time scale, over which the laser was scanned, to a frequency scale is needed. To do this the data from the FPI recorded simultaneously with the spectra is used. The FPI data for each spectrum is split up in separate FPI scans using the trigger ramp signal as indicator of the start and stop of each scan. One such scan can be seen in figure 4.1. Then both the HeNe and Ti:Sa peak positions in a scan are identified.

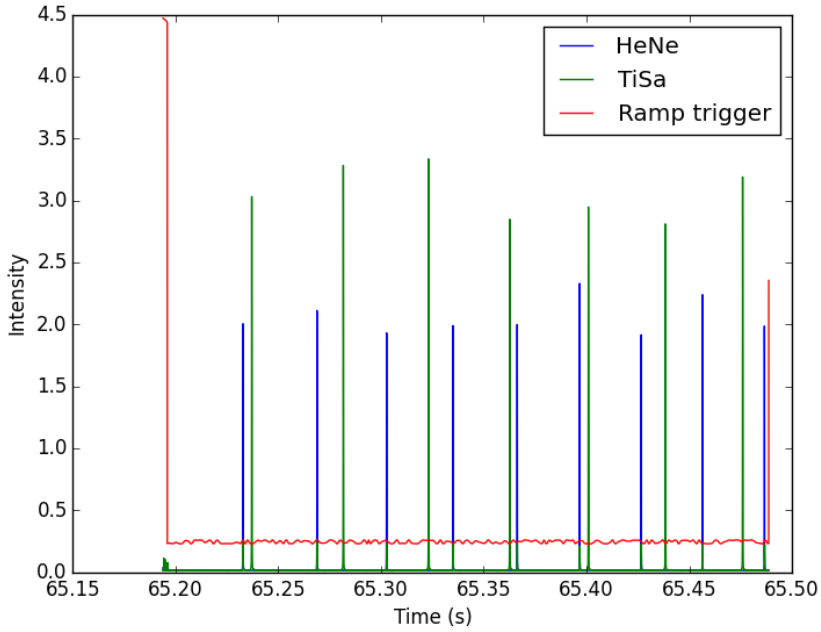

Figure 4.1: One scan of one of the recorded FPI spectra.

In a perfect FPI, the distance between two peaks of one laser (the FSR) should be constant, but in reality this is not the case due to nonlinearity of the piezo scanning of the mirror. Therefore, a linearization of the peak positions is made. The positions of the HeNe peaks, with the first peak set to zero for reference, are plotted versus the number of peaks counted so far, which is equal the number of scanned FSRs. The data points are then fitted with a linear, quadratic and cubic polynomial. An example of one such fit can be seen in figure 4.2. As expected, due to the non-linear effects introduced by the scanning of the piezo, a linear fit does not reproduce the data correctly. The cubic fit is the best choice, the data is reproduced accurately to about 1% (determined from the residuals). Higher order polynomials did not significantly improve the fit.

For verification, the positions of the Ti:Sa peaks of this one scan were converted to "number of FSR", using the fit parameters determined from the fit of the HeNe peaks. The results have to be scaled by the ratio of the wavelengths $\lambda_{HeNe}/\lambda_{Ti:Sa}$ to yield the true FSR numbers of the Ti:Sa peaks. The wavelength of the Ti:Sa is taken as 794.979 nm, the value to which the laser cavity is referenced. The scanning of the laser will introduce a small error, but this is not taken into account here. The difference between the succeeding "number of FSR" obtained should then be equal to one, as the difference between the calibrated and rescaled Ti:Sa peak positions should be equal to one FSR. For seven Ti:Sa peaks the mean difference was 0.9959. This suggests a remaining error for the non-linearity of $< 0.2\%$ of one FSR or about 2 MHz.

The linearization using a cubic fit is done for each FPI scan in a data file. The linearized Ti:Sa peak positions can then be used to determine the frequency. In each FPI scan the positions of the HeNe peaks remain fixed as the frequency of this laser does not change. The positions of the Ti:Sa peaks however will shift from one scan to another as the frequency is scanned. The time difference $(peak_{Ti} - peak_{He})$ between a HeNe transmission fringe $(peak_{He})$ and a Ti:Sa fringe $(peak_{Ti})$ are tracked in each data file.

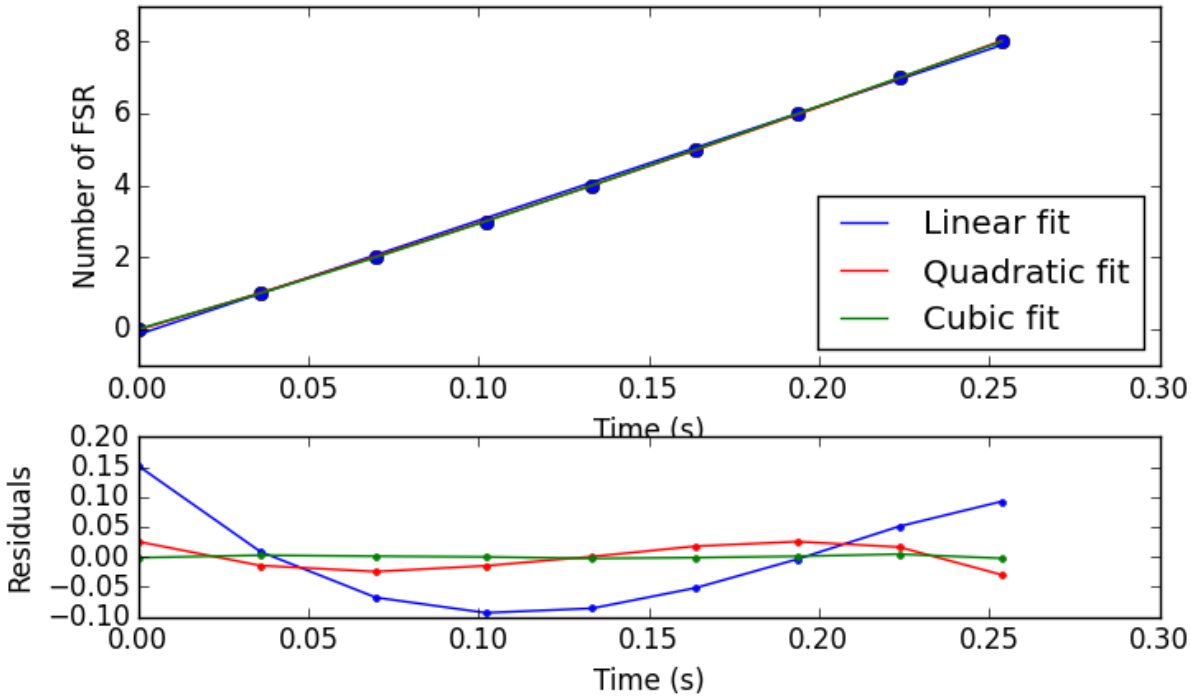

Figure 4.2: Upper panel: relative timing of HeNe peaks against FSR number with the first peak set to zero for reference. The curves are fits to the data. Lower panel: residuals of the fits to the timing data of the HeNe peaks.

The change in relative timing difference between the Ti:Sa and HeNe fringe is proportional to the frequency change between scans. As the scan range of the Ti:Sa is about 10 GHz, it spans multiple FSRs, so the tracked Ti:Sa peak would at some point leave the available scanning range provided by the piezo. To overcome this problem, the tracking in the analysis procedure jumps back by one Ti:Sa fringe each time the currently tracked Ti:Sa peak moves too far apart from the HeNe fringe, i.e. by more than one half of an FSR. The frequency change can then be calculated as

$$\Delta\nu = \frac{peak_{Ti} - peak_{He} + N_j \cdot FSR_{Ti}}{FSR_{Ti}} \cdot FSR_{FPI} \tag{4.2}$$

where N_j is the number of jumps, FSR_{Ti} is the timing difference between two Ti:Sa peaks and FSR_{FPI} is the FSR of the FPI in frequency which is 1 GHz. These frequency differences are then stepwise added together to determine the full frequency range and exported together with the time axis to use in the analysis of the saturation spectra.

4.3 Dependence on power

The linewidth of the saturation peaks depends on the overall power of the laser and on the ratio between the power of the pump and probe beam, as can be seen in eq. 2.38. For all scans used in the analysis, the overall power has been kept constant at 810 mW directly after the laser and about 53 μW for the probe beam. This is the maximum as the photodiodes reach their readout limit. The power ratio between the pump and probe

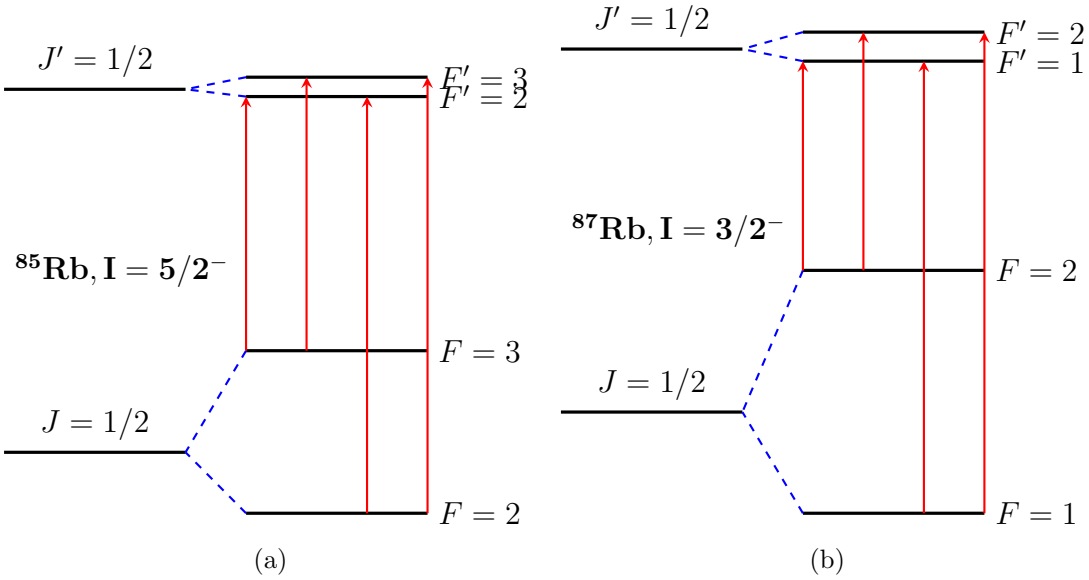

Figure 4.3: D1 line in rubidium and hyperfine splittings.

beam was varied by introducing different filters into the pump beam after the telescope. The pump beam power varies from about 140 μW to 5.3 mW for the eight different scans. The spectra for all different pump beam powers can be found in appendix A.

First of all the spectra are fitted with a hyperfine structure with parabolic background (ax^2+bx+c). The hyperfine structure and allowed transitions of the D1 line in Rb can be seen in figure 4.3. The fit uses a Lorentzian profile for the line shape of the resonances as any Gaussian contribution due to residual Doppler broadening is negligible. The positions of the resonances are determined by using the formulas 2.19 and 2.20

$$\nu_i = \nu_0 + \frac{A_{85}(^2P_{1/2})C_i}{2} - \frac{A_{85}(^2S_{1/2})C_i}{2} \tag{4.3}$$

$$\nu_i = \nu_0 + \nu_{87-85} + \frac{A_{87}(^2P_{1/2})C_i}{2} - \frac{A_{87}(^2S_{1/2})C_i}{2} \tag{4.4}$$

where ν_0 is the fine structure transition frequency between the lower level $^2S_{1/2}$ and upper level $^2P_{1/2}$, called the center of gravity or centroid frequency, of ^{85}Rb, ν_{87-85} is the isotope shift between ^{87}Rb and ^{85}Rb and the A's are the hyperfine parameters. For each isotope four transitions are allowed as can be seen in figure 4.3, which leads to eight peaks. There are crossover peaks to consider, as the transitions with a common lower level overlap within their Doppler width. This results in four crossover peaks with their centroids determined by the centroids of the overlapping transitions ($\nu_i = (\nu_1 + \nu_2)/2$).

This gives nine fitting parameters, namely the centroid, isotope shift, the four hyperfine parameters and the three parameters for the parabolic background. Twelve more parameters are needed to account for the intensity of each peak. The last one is the FWHM which is taken to be common for all peaks. This results in a total of 22 fitting parameters. To reduce the number of parameters, one can consider using the Racah relative intensities (eq. 2.24). This reduces the number of fitting parameters to 16 as only six parameters for the intensities are used, one for the peaks from ^{85}Rb, one for the peaks from ^{87}Rb and one for each of the four crossover peaks.

The spectra are fitted with a script written in Python based on the lmfit fitting package [40]. This package uses non-linear least-squares fitting to minimize the χ^2 value. This value gives the difference between the measured values n_i and the theoretical prediction given by the fit function $f_i(x)$, weighted by the errors on the measurement ϵ_i

$$\chi^2 = \sum_i^N = \frac{(n_i - f_i(x))^2}{\epsilon_i^2} \tag{4.5}$$

Here N is the number of datapoints and x represents the fit parameters. The errors ϵ_i are given by the statistical errors due to averaging of the data points, as explained in the previous section. For a good fit χ^2 should be roughly equal to the number of degrees of freedom d, defined as the number of datapoints N minus the number of fit parameters. This can also be expressed by the reduced chi-square $\chi^2_{red} = \chi^2/d$ that should be around 1. When the χ^2_{red} is reasonably bigger, the proposed fit parameters are still accepted if the fitting function is believed to be correct. In this case, the errors on the parameters determined during the fitting procedure are multiplied by the square root of the reduced chi-square. This multiplied error is then the statistical error on the parameter which corresponds to a 68% (1σ) confidence level.

The first fit of the spectra, using free intensities, is done with the time as x-values. This is only used to determine the time position of the centroid in each scan. As stated before, the frequency determined from the FPI is not absolute and needs a reference point. Here the centroid of the hyperfine structure is used as a reference. The frequency scale is shifted to have a value of zero at the time position of the centroid. Then the time axis is substituted by the frequency axis.

The spectra are fitted again, once with free intensities and once with using Racah relative intensities and using the known hyperfine parameters, centroid and isotope shift (fig. 4.3) as starting parameters. The parameters are not fixed as some remaining nonlinearity could have a small influence. This is indeed the case as the fit parameters do not always coincide with the literature values, as can be seen in table 4.1.

In some scans the statistics for the ^{87}Rb are quite low, which can have an influence on the common FWHM that is needed for further analysis. It was therefore decided to limit the spectra to the central ^{85}Rb peaks and fit those with a common FWHM. The results for the FWHM of these fits can be found in table 4.2, with the statistical error calculated as explained before. The fits with free intensities can also be found in appendix A. The fits with Racah relative intensities were not included as the visual difference is very small. The FWHM for scan 3 is unusually high. This is probably due to the low intensities of the peaks and the remaining non-linearity in the frequency determination. The peaks are thus not spaced perfectly, and the fitting routine compensates by broadening the FWHM.

The FWHM can now be plotted against the pump power for each scan. This should follow the formula 2.38, so it is fitted with the equation

$$FWHM = \gamma_{nat}\sqrt{1 + I * pump} + b \tag{4.6}$$

where $\gamma_n at = 5.7500(56)$ MHz is the natural linewidth of the transition [5, 6]. The formula has two fitting parameters, I which is related to the saturation parameter S_0, and b which should give the power broadened linewidth by the probe beam. The outlying value of the FWHM of scan 3 is taken out as it had too much impact on the fit result. The fits can be seen in fig. 4.4 and 4.5. The resulting χ^2_{red} is 5.419 for the Racah intensities values

		χ^2_{red}	$A_{85,u}$ (GHZ)	$A_{85,l}$ (GHZ)	$A_{87,u}$ (GHZ)	$A_{87,l}$ (GHZ)	ν_{87-85} (GHZ)
Scan 1	Racah	2.402	0.1216(6)	1.0127(5)	0.413(2)	3.428(2)	0.078(2)
	Free	2.364	0.1214(6)	1.0127(5)	0.4133(17)	3.428(2)	0.077(2)
Scan 2	Racah	2.242	0.1143(5)	1.0128(5)	0.4121(14)	3.427(2)	0.074(2)
	Free	2.214	0.1142(5)	1.0127(5)	0.4119(13)	3.427(2)	0.074(2)
Scan 3	Racah	2.170	0.1249(12)	1.012(2)	0.415(4)	3.421(5)	0.072(5)
	Free	2.135	0.1251(13)	1.0117(14)	0.415(4)	3.421(5)	0.072(4)
Scan 4	Racah	1.935	0.1165(4)	1.0131(4)	0.4121(9)	3.426(2)	0.0766(14)
	Free	1.923	0.1165(4)	1.0131(4)	0.4120(9)	3.426(2)	0.0766(14)
Scan 5	Racah	1.513	0.1170(5)	1.0128(4)	0.4072(8)	3.4265(14)	0.0761(13)
	Free	1.367	0.1171(4)	1.0128(4)	0.4086(8)	3.4269(11)	0.0766(10)
Scan 6	Racah	1.465	0.1167(3)	1.0133(3)	0.4107(6)	3.4244(13)	0.0749(11)
	Free	1.451	0.1167(3)	1.0133(3)	0.4108(6)	3.4243(14)	0.0749(11)
Scan 7	Racah	2.153	0.1152(5)	1.0132(4)	0.4111(11)	3.425(2)	0.074(2)
	Free	2.119	0.1151(4)	1.0131(4)	0.4111(11)	3.4244(14)	0.0742(13)
Scan 1	Racah	1.641	0.1171(4)	1.0136(4)	0.4094(7)	3.424(2)	0.0746(13)
	Free	1.609	0.1170(4)	1.0137(3)	0.4093(7)	3.4239(13)	0.0742(12)

Table 4.1: Results for hyperfine parameters from fitting the saturation spectra. The literature values for the parameters are $A_{85,u} = 0.120527(56)$ GHz, $A_{85,l} = 1.0119108130(20)$ GHz, $A_{87,u} = 0.40724(77)$ GHZ, $A_{87,l} = 3.417341305452145(45)$ GHz and $\nu_{87-85} = 0.078095(12)$ GHz [5, 6].

	Pump power (mW)	Intensities	χ^2_{red}	FWHM (MHz)
Scan 1	0.64(3)	Free	2.196	47.3(18)
		Racah	2.236	46.5(18)
Scan 2	0.37(2)	Free	2.133	34.4(19)
		Racah	2.163	34.1(19)
Scan 3	0.140(7)	Free	1.553	49.6(22)
		Racah	1.772	43.4(18)
Scan 4	1.62(9)	Free	1.885	43.1(12)
		Racah	1.894	43.3(12)
Scan 5	5.3(3)	Free	1.378	60.8(9)
		Racah	1.517	60.6(9)
Scan 6	3.4(2)	Free	1.504	53.4(7)
		Racah	1.527	53.2(7)
Scan 7	2.3(1)	Free	2.137	45.9(15)
		Racah	2.164	46.1(15)
Scan 8	4.7(2)	Free	1.612	58.5(11)
		Racah	1.646	58.4(11)

Table 4.2: Results for FWHM from fitting the saturation spectra of ^{85}Rb.

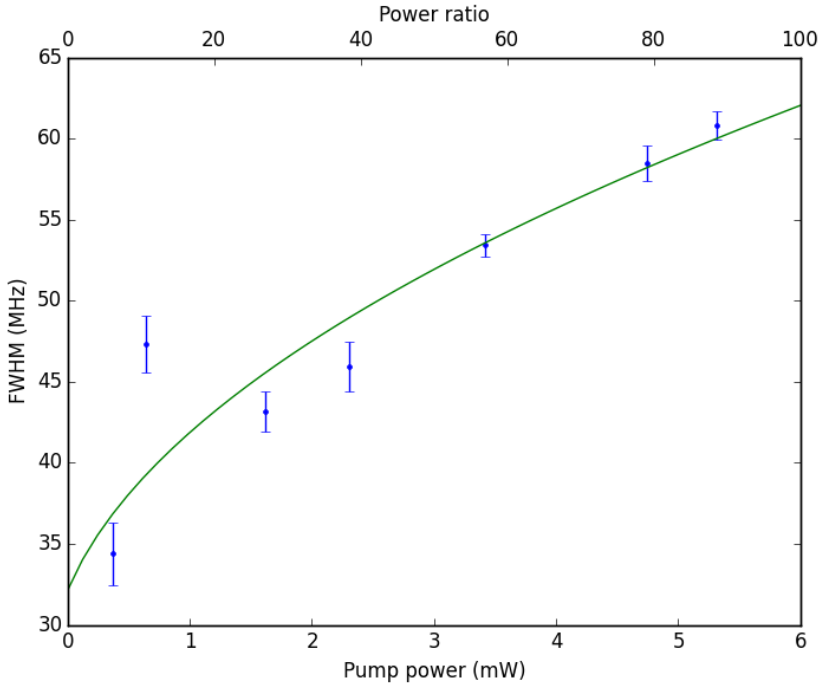

Figure 4.4: FWHM plotted against power ratio with fit following eq. 4.6. The ratio of pump to probe power is added as reference.

and 6.235 for the free intensities values. For the Racah values the fit parameters are $b = 26(3)$ MHZ and $I = 6.3(17)$ 1/mW, for the free intensities values $b = 26(4)$ MHz and $I = 6.2(18)$ 1/mW. These values are strongly correlated, as can be seen in the plots of the confidence intervals fig. 4.6 and 4.7. This correlation was to be expected from the fit formula, as a larger curvature (related to parameter I) results in a lower offset (parameter b).

It is now possible to compare the offset parameter b, to the expected saturation broadening by the probe beam. The probe beam has a power of about 53 μW and a diameter of about 1 mm, which gives an intensity of about 6.7 mW/cm^2. The saturation intensity of the D1 transition is 4.4876(31) mW/cm^2. Using formula 2.38, the power broadened linewidth should be about 9.08 MHz. This is only a crude estimate, but clearly lower than the results for the offset parameter b, so there is residual broadening. This is most likely due to artificial broadening in the fitting routine due to imperfect conversion to frequency.

4.4 Characterization of FPI

4.4.1 Determining the free spectral range

In the analysis described in the previous section, an FSR of 1 GHz was assumed, as stated by the technical specifications of the FPI. However, this is not always an accurate value. Using the hyperfine spectra it is possible to make a more accurate determination of the FSR. The FSR will influence the frequency spacing between points, thus when taking the

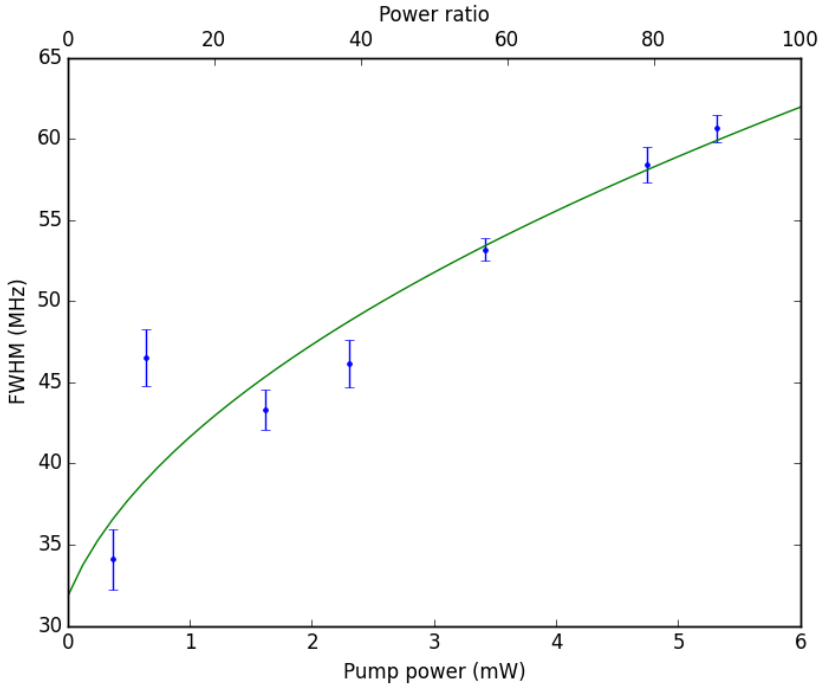

Figure 4.5: FWHM plotted against power ratio with fit following eq. 4.6. The ratio of pump to probe power is added as reference.

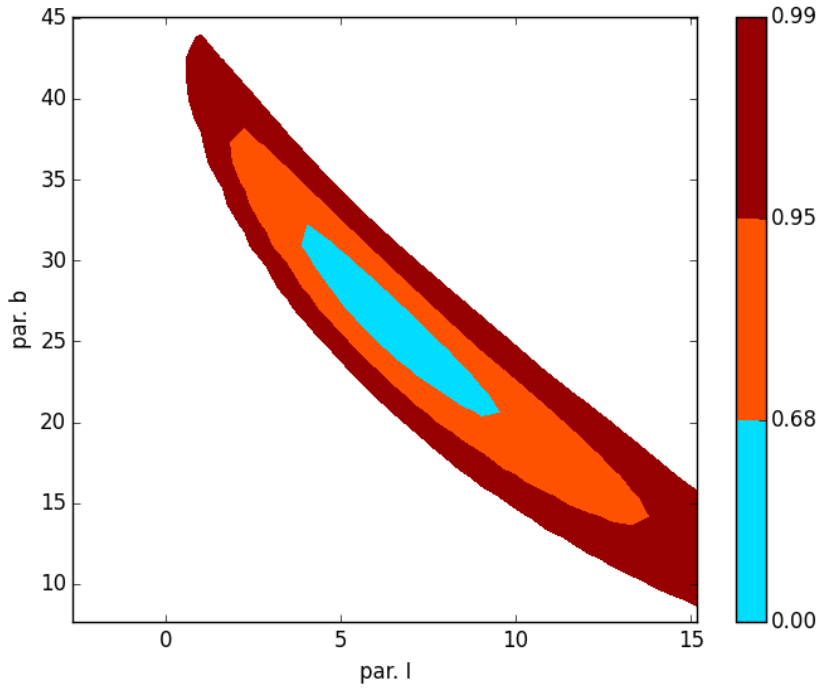

Figure 4.6: Confidence intervals plotted as function of the two fit parameters when using free intensities. The correlation is clearly visible.

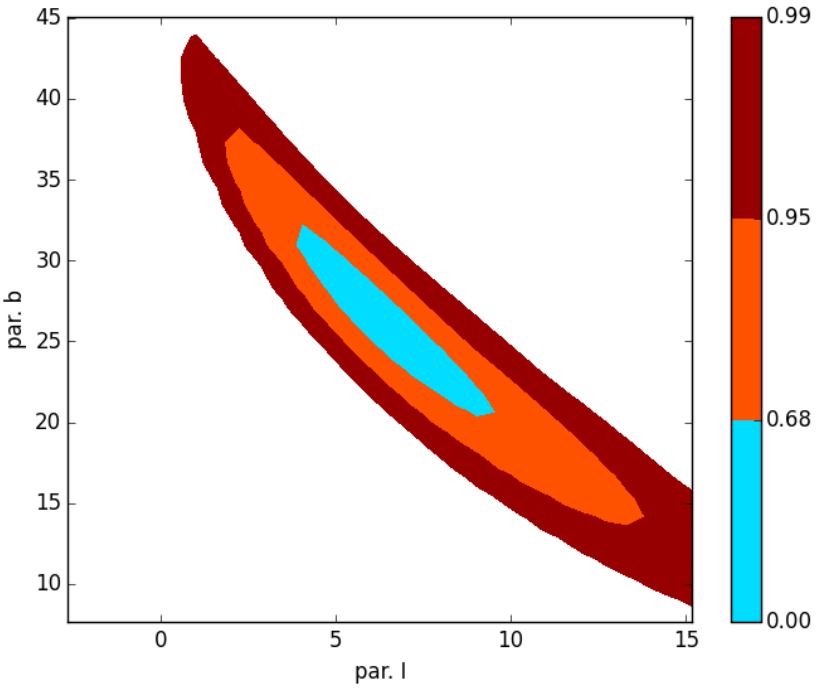

Figure 4.7: Confidence intervals plotted as function of the two fit parameters when using Racah intensities. The correlation is clearly visible.

centroid of a hyperfine structure as reference, changing the FSR will expand or shrink the hyperfine structure. To quantify this, a fit with the hyperfine parameters fixed to the known values but introducing a common scaling factor for all of them can be done. The inverse of this scaling factor is an accurate measure of the FSR. The centroid is still left as fitting parameter to account for a possible misfitting of the centroid before. The fit then has 12 fitting parameters when using Racah relative intensities, the 3 background parameters as before, the FWHM, the centroid, the 6 intensities and the scaling factor. An example of one such fit can be seen in figure 4.8. The results for each scan can be found in table 4.3. As these can be considered as independent measurements of the same quantity, the FSR, the formula for the weighted mean applies [41]:

$$\langle FSR \rangle = \frac{\sum_i FSR_i/\epsilon_1^2}{\sum_i 1/\epsilon_1^2} \tag{4.7}$$

The error on the weighted mean is usually calculated as

$$\epsilon_{stat}^2 = \frac{1}{\sum_i 1/\epsilon_1^2} \tag{4.8}$$

When there is considerable scattering in the measured values, this statistical uncertainty does not represent the true uncertainty. The error is then specified better by

$$\epsilon_{scat}^2 = \frac{1}{1-\sum_i \varepsilon_i^4} \frac{1}{N} \sum_i^N \frac{(FSR_i - \langle FSR \rangle)^2}{\varepsilon_i^2} \tag{4.9}$$

where N is the number of measurements, here 8, and ε_i are the normalized errors such that $\varepsilon_i^2 = \epsilon_i^2 / \sum_i \epsilon_i^2$. This results in an FSR of 0.998(5) GHz. When only considering the

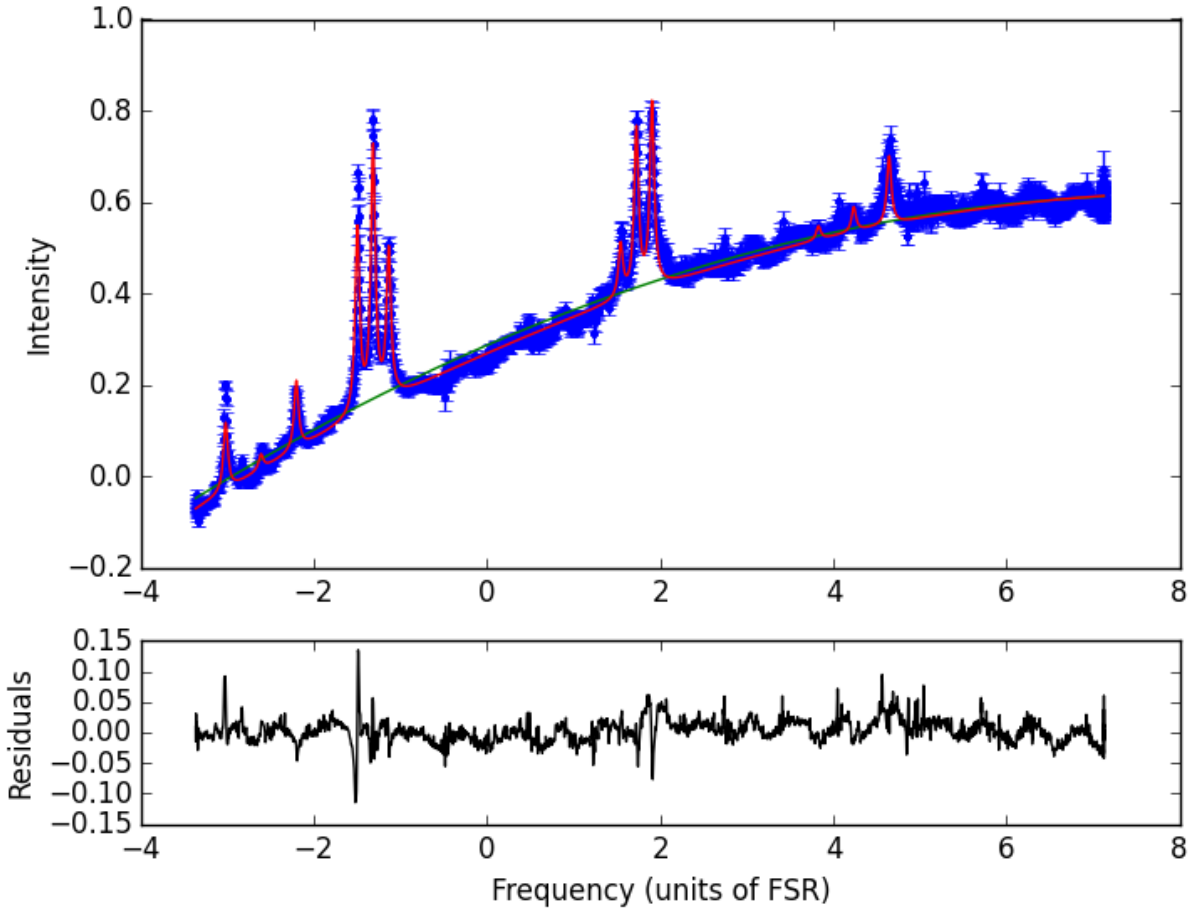

Figure 4.8: Fit of scan 5 using hyperfine structure with common scaling factor, Racah relative intensities and a parabolic background. The top panel is the spectrum with the background fit in green and the total fit in red. The bottom panel are the residuals.

statistical error, the result is in an FSR of 0.99793(12) GHz, which is slightly lower than the specified value of 1 GHz. But even with only the smaller statistical error, the value is in accordance with the previous calibrated value of 0.99850(15) GHz [7].

4.4.2 Determining the finesse

As stated before, the finesse of an etalon or FPI is defined as the ratio of the free spectral range to the FWHM of the resonances. As the FWHM of the resonances must be measured, the peaks must contain enough data points to allow fitting of Lorentzian profiles. In all the data files mentioned so far the scan rate of the piezo was too fast to allow this. The finesse is thus determined from a separate scan with a slower scanning rate.

The incomplete scan and the two complete scans are fitted separately with Gaussian profiles and one common FWHM per scan. A Gaussian profile was chosen as approximation to the Airy function because it gave better fitting results than a Lorentzian, as can be seen in fig. 4.9. The last peak of each scan is not taken into account as it is too close to the trigger signal which can disturb the piezo mirror. The results for the FWHM of each fit can be seen in table 4.4. The mean of these three values is taken and the error is deter-

	χ^2_{red}	FSR (GHz)
Scan 1	2.351	0.9982(4)
Scan 2	2.293	0.9982(4)
Scan 3	2.162	0.9966(12)
Scan 4	1.924	0.9989(3)
Scan 5	1.768	0.9975(3)
Scan 6	2.161	0.9971(3)
Scan 7	2.198	0.9990(3)
Scan 8	2.027	0.9967(3)

Table 4.3: Results for the FSR determined from fitting with a scaling factor.

FWHM (ms)
1.390(7)
1.354(7)
1.278(8)

Table 4.4: Results for the FWHM of the FPI transmission peaks.

mined from the three statistical errors by the formula for error propagation, resulting in FWHM = 1.341(4) ms. The FSR is taken as the average over all the differences between consecutive peaks with a corresponding standard error, FSR = 0.54(4) s. The finesse is then calculated to be $F^* = 400(28)$, close to the specified minimum of 400. Using formula 2.17, the reflectivity of the mirrors can be calculated to be about 99.2%.

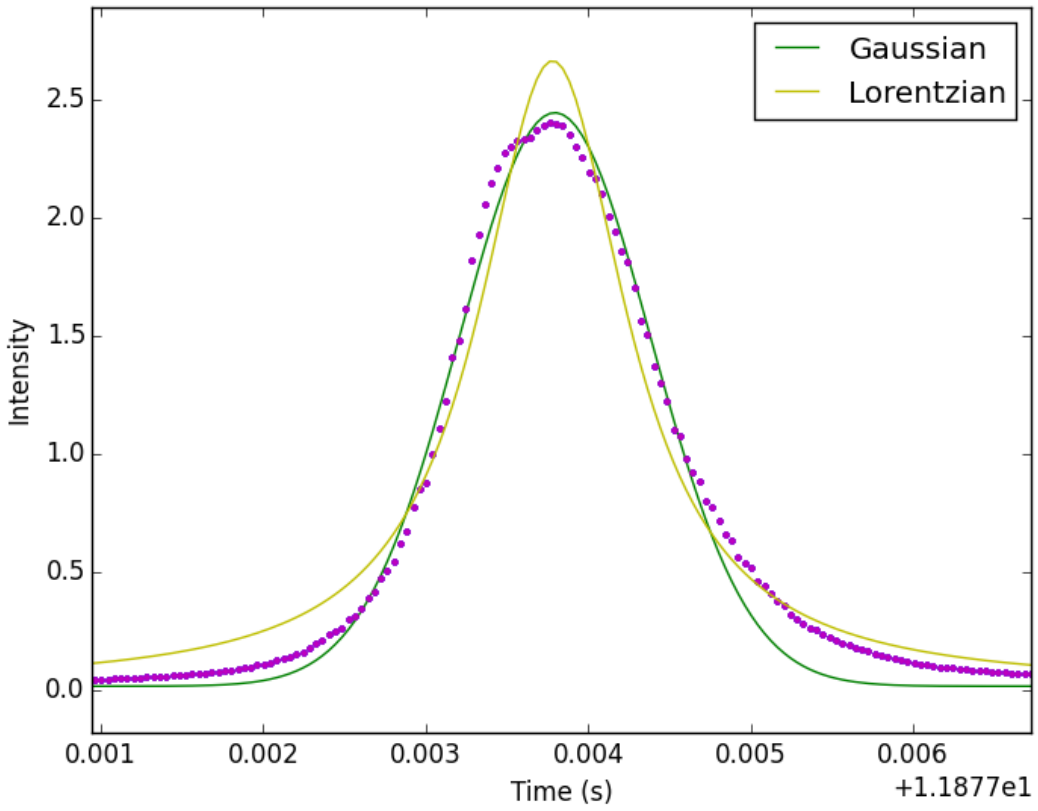

Figure 4.9: Fit of one FPI transmission peak with a Gaussian and a Lorentzian profile.

Chapter 5

Towards collinear laser spectroscopy of ^{42g,m}Sc

Participation in the collinear laser spectroscopy experiment on ^{42}Sc at IGISOL was part of the work done for this thesis. There were technical problems however hindering the experiment. Adding to this the fact that a spectrum would be quite complex with numerous peaks due to the $I = (7)$ isomer and the $J = 2 \rightarrow J = 3$ transition, explains why no usable results were obtained from this experiment. As it is still a very interesting case, the motivation for the experiment will be discussed in this chapter.

5.1 Motivation

The motivation to study ^{42g,m}Sc is most easily seen by looking at the occupation of proton and neutron shells in figure 5.1. ^{42g,m}Sc has 21 protons and 21 neutrons, making it an $N = Z$ nucleus with one proton and one neutron more than the doubly magic ^{40}Ca. A short introduction on the shell-model will be given in the next section. The odd-odd $N = Z$ nuclei provide an ideal testing ground for isospin symmetry and pairing correlations as the odd proton and neutron occupy the same shell and thus have the same nuclear wavefunction. The isospin quantum number will be explained in the second section.

As it is at the same time a neighbor of the doubly magic nucleus ^{40}Ca, studying ^{42g,m}Sc can give information on the 'softness' of this core, in other words the strength of the magic number 20 in this nucleus. Nuclear properties in the neighborhood of magic numbers are often single-particle in nature and thus provide a strict test for the ability of theoretical models to reproduce and predict experimental observables. In the last section a short overview of what is already known about ^{42g,m}Sc and neighboring isotopes will be presented, together with what could be learned from a collinear laser spectroscopy experiment on this isotope.

5.1.1 The nuclear shell model

The nuclear shell model in its original form [36] was founded on the success of the atomic shell model, called the Bohr model, and experimental data of ground state (g.s.) properties such as mass, spin-parity and magnetic moments that supported the existence of nuclear shells because of sudden discontinuities at certain proton and neutron numbers. These

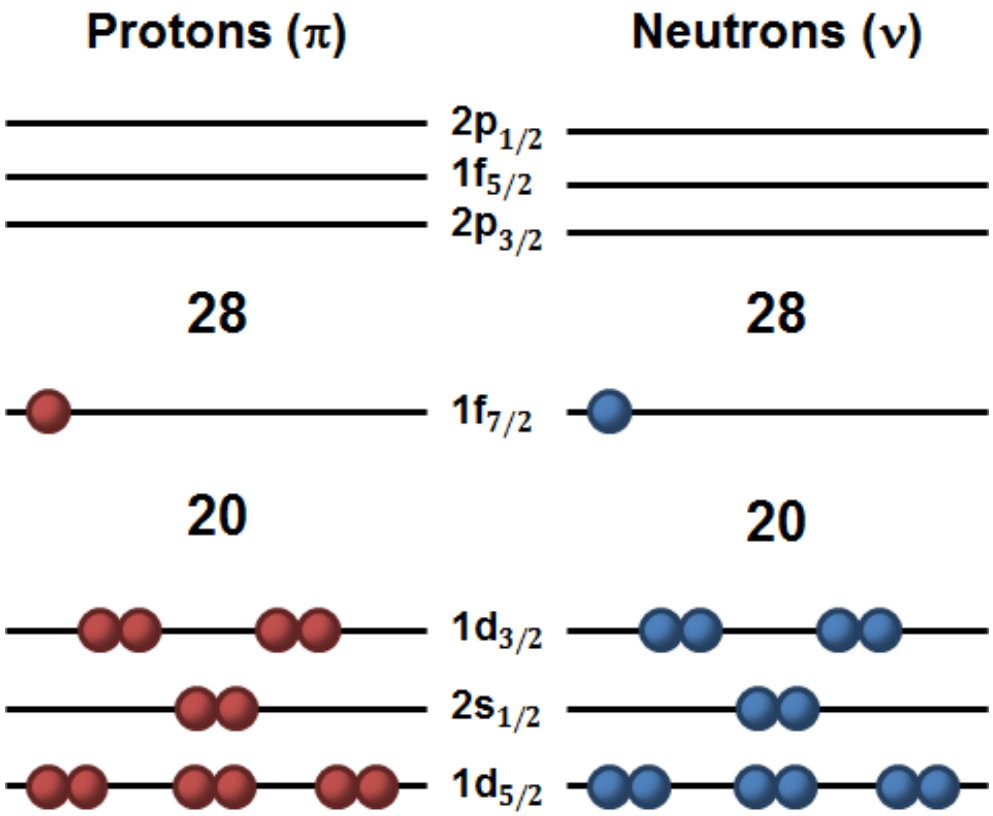

Figure 5.1: The configuration of the proton and neutron shells for ^{42g,m}Sc.

numbers become known as the 'magic numbers' and represent the effects of filled major shells. The most important difference between the nuclear shell and Bohr model is the potential in which the particles move. In the atomic model, the electrons move in a well-defined Coulomb potential generated by the nucleus. In a nucleus, the nucleons move in a potential that they create themselves. The fundamental assumption of the shell model is that the motion of a single nucleon is governed by a potential caused by all of the other nucleons. This central potential includes a basic part, a harmonic oscillator or Woods-Saxon potential, and a spin-orbit potential. The single-particle motion in this potential can be solved, resulting in energy eigenstates which are called single-particle orbits [24]. These orbits are characterized by the radial quantum number n, the orbital momentum l and the total angular momentum j. The eigenstates are grouped in shells with degeneracy $2j + 1$ and large energy gaps between them, accurately reproducing the magic numbers observed experimentally.

In the extreme limit, the shell model asserts that only the single unpaired nucleon determines the properties of the nucleus, such as the g.s. spin, parity and nuclear moments. This gives correct predictions for nuclear properties of odd-A nuclei in the neighborhood of magic numbers. It was soon realized however that all valence nucleons and the interaction between the valence nucleons and the core (completely filled shells) had to be taken into account to make accurate predictions. The basic shell model is extended with a residual, effective, interaction between the valence nucleons. This modifies the single particle energies (SPE) resulting in effective single-particle energies (ESPE).

One way to calculate these ESPE's is by using large scale shell model calculations. These calculations are based on the choice of an appropriate core of closed shells combined with a configuration space in which the valence nucleons can interact via an effective interaction. This effective interaction must be adapted to the chosen valence space and is usually determined (partially) phenomenologically.

5.1.2 Isospin

The charge independence of nuclear forces, deduced from nucleon-nucleon scattering data, means that in most cases there is no need to distinguish between neutrons and protons in the formalism. Instead they are grouped together and called 'nucleons'. The formalism for nuclear interactions may depend on the multiplicity of nucleon states (two) but is independent of whether the nucleons are protons or neutrons. This symmetry holds of course only for the strong (nuclear) force, the electromagnetic interaction does distinguish between protons and neutrons. This two-state degeneracy gave rise to a formalism analogous to that of the magnetic interaction of a spin-$\frac{1}{2}$ particle, as the spin orientation/projection of a particle also does not influence the nuclear physics formalism but comes into play when a magnetic field is applied. The neutron (ν) and proton (π) are treated as two different states of a singe particle, the nucleon. The nucleon is assigned a fictitious spin vector, called the isospin, with a magnitude t of $\frac{1}{2}$. The proton is then arbitrarily assigned 'isospin-up' ($m_t = +\frac{1}{2}$) and thus the neutron 'isospin-down' ($m_t = -\frac{1}{2}$).

Even though it is an arbitrary construction, the isospin obeys the usual rules for angular momentum vectors. The isospin vector $\mathbf{t}$ thus has a length of $\sqrt{t(t+1)}\hbar$ and a third-axis projections (similar to the z-axis, but arbitrarily chosen) $t_3 = m_t\hbar$ [24]. For a system of several nucleons the isospin follows the coupling rules of ordinary angular momentum vectors. For example, a two-nucleon system can have total isospin T of 0 or

1, corresponding (semiclassically) to the antiparallel or parallel orientations of the two isospin-$\frac{1}{2}$ vectors. The third-axis component of the total isospin vector, T_3, is the sum of the third-axis components of the individual nucleons, and thus for any nucleus

$$T_3 = \frac{1}{2}\hbar(Z - N). \tag{5.1}$$

When looking at a two-nucleon system it is clear that this can have either $T = 0$ or $T = 1$. This leads to four possible third-axis components: $T_3 = +1$ ($\pi\pi$), $T_3 = -1$ ($\nu\nu$) and two combinations with $T_3 = 0$ ($\pi\nu$ or $\nu\pi$). If the nuclear interactions are indeed perfectly charge independent and the electromagnetic interactions is ignored, the three third-axis projections of $T = 1$ must have the same energy, while the single $T = 0$ state may have a different energy. This is evidenced by the fact that the isospin triplet, which is the $I = 0$ singlet of ordinary spin, is unbound. The deuteron is the bound $T = 0$ singlet.

It is thus also possible to assign an isospin quantum number to nuclear states. The tendency towards nuclear symmetry implies that the lowest states will most likely have $T = |T_3|$. This gives a good first guess for the isospin of the ground state, and excited states can be assigned on the basis of reaction or decay studies or symmetry arguments because angular momentum coupling theory leads to selection rules for dipole transitions. These are that ΔT must be 0 or ± 1, except that $T = 0$ to $T = 0$ transitions are forbidden as well as $\Delta T = 0$ transitions in $T_3 = 0$ nuclei [24]. As already explained before, $\pi\nu$ pairs with $T = 1, T_3 = 0$ should be treated on an equal footing to the $T = 1$ $\pi\pi$ and $\nu\nu$ pairs with $T_3 = +1, -1$ respectively. This means that in nuclei with the same mass and two unpaired nucleons but one proton or neutron interchanged there should be levels with the same energy, called isobaric analog states. These analog states in neighboring nuclei have identical nucleon wave functions except for the change in proton and neutron number and can for example be found in the $A = 42$ mass system as can be seen in figure 5.2. The energies have to be adjusted by small amounts to account for the neutron-proton mass difference (an electromagnetic effect) and the Coulomb energy of the nucleus.

5.1.3 ^{42g,m}Sc and neighboring isotopes

As can be seen from fig. 5.2, ^{42}Sc has a $I = 0$ ground-state with lifetime 681.3 ms [21] as the odd proton and neutron couple antiparallel. The atomic spectrum of the ground-state will thus not have a hyperfine structure and no nuclear moments can be measured. There is however a long-lived excited state, an isomer, at 616.28 keV with $I = (7)$ [21], as the odd proton and neutron in the $f_{7/2}$ shell couple parallel. The lifetime is 61.7 s [21], long enough to allow collinear laser spectroscopy. This isomer will exhibit a hyperfine structure, so nuclear moments could be derived. If ^{40}Ca would be a perfect core, the nuclear moments would be single-particle in nature, only determined by the coupling of the moments of the odd proton and neutron. However, it has been demonstrated before that ^{40}Ca is not a perfect core, as excitations across the shell gaps were needed to accurately reproduce the measured data. This was for example needed to reproduce the level scheme of ^{42}Sc in [19], to calculate M1 strengths in ^{36,38}Ar in [22] and to reproduce the isomer shift in ^{38}K [23]. The nuclear moments of ^{42m}Sc could give a further indication of the strength of the shell closures at the magic number 20 and thus provide input for effective shell model interactions that are used in the region around ^{40}Ca.

The isomer shift $\delta\nu^{42m,42g}$ could also provide valuable information about proton-neutron pairing. The structure of ^{42}Sc is similar to the one of ^{38}K, which has one hole

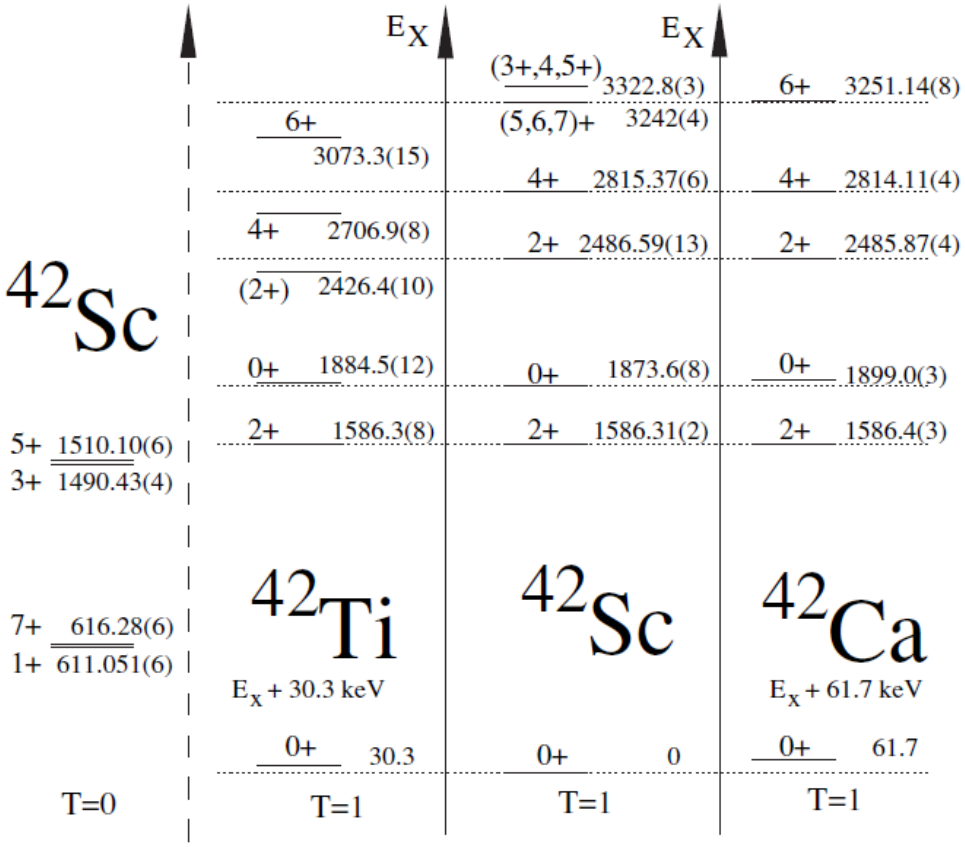

Figure 5.2: $T = 1$ isospin multiplets in ^{42g,m}Ti, ^{42g,m}Sc, and ^{42g,m}Ca up to an excitation energy of 3.3 MeV. The levels in ^{42g,m}Ti and ^{42g,m}Ca are shifted relative to the ^{42g,m}Sc levels by 30.3 and 61.7 keV, respectively, to match the excitation energy of the first 2^+ ($T = 1$) levels. The lowest $T = 0$ states in ^{42g,m}Sc up to 1.5 MeV are also shown in the left part of the figure [19].

in the proton $d_{3/2}$ shell and one hole in the neutron $d_{3/2}$ shell. The isomer shift in this isotope has already been measured and studied in [23] with a corresponding difference in mean square charge radii between the $I = 3$ ground state and the $I = 0$ isomer. There is an increase in size for the isomer, remarkably larger than the odd-even staggering observed in ground-state mean square charge radii. When plotting the differences in charge radii as a function of A along the line of $N = Z$, it was seen that the larger charge radius of the ^{38}K ($T = 1$) isomer is consistent with a smooth increase in size along the $N = Z$ line, while the ground-state is somewhat smaller than the average of its two neighbors.

This could be explained by looking into the effect that causes the odd-even staggering of the ground-state mean square charge radii. In even nuclei, the $I = 0$ pairs of protons or neutrons scatter to a large number of states near the highest occupied state. This increases the mean square charge radius of the even-even isotopes as compared to that of its even-odd neighbors. An extra odd proton or neutron 'blocks' a specific state and thus reduces the scattering of the pairs, making the odd isotopes somewhat smaller than their even neighbors. As discussed in section 5.1.2 however, proton-neutron pairs should be considered on an equal footing as proton-proton and neutron-neutron pairs. In the case of ^{38}K, this means that for the $T = 1$ isomer, the $\pi\nu$ pair coupled to $I = 0$ is free to scatter into a range of orbitals, making the isomeric radius effectively bigger than the $T = 0$, $I = 3$ ground state radius and putting it on an equal footing with the even neighbors.

In ^{42}Sc the picture is somewhat different as the states are 'reversed'. The ground state is now $I = 0$ and $T = 1$ while the isomer is $I = (7)$ and $T = 0$. Following the same reasoning as for ^{38}K, it is thus expected that the isomer will be smaller in size than the ground state. A reduction of the mean square charge radius of the isomer compared to the ground state has already been observed in some multi-quasi particle nuclei [39]. There it is assumed that the same effect as explained here, the orbital blocking of the odd nucleon, causes the increase in rigidity and decrease in surface diffuseness needed to explain the measured quantities.

Chapter 6

Conclusion and outlook

This thesis reported on the work done towards the development of a saturated absorption spectroscopy setup at IGISOL. Besides technical improvements, the dependence on pump beam power of the saturation spectra and the properties of the FPI were investigated. The results from the dependence on pump beam power of the saturation spectra showed influences from imperfections in the fitting procedure, most likely due to imperfections in the conversion to frequency. This could be further investigated, as well as the dependence of the spectra on the probe beam power. The measured properties of the FPI, the free spectral range and the finesse, are in accordance with the technical specifications of the FPI and can be used in future analysis of data obtained using the setup.

The setup will be used in the near future for the calibration of other FPIs, especially home-made FPIs. Another goal is to make an electronic feedback from the setup to the HeNe laser to check its long-term stability, which is needed if the HeNe laser would be used in a stabilization scheme for the cw Ti:Sa laser. In the future the cw Ti:Sa laser would be used for collinear laser spectroscopy experiments on neutral atoms. For those experiments the laser frequency needs to stable both on short and on long time scales. In the current configuration this is not the case, there is only an external fiber-coupled reference cavity for short-term frequency stabilization which is susceptible to temperature drifts leading to long-term frequency drifts. Techniques to ensure long-term stabilization are thus needed. Locking to a fixed frequency can for example be achieved by referencing to an atomic transition and using a feedback loop to adjust the laser when necessary. This is possible using saturated absorption spectroscopy, with a setup as described in this thesis. More flexible wavelength stabilization is possible using a scanning FPI and a frequency-stabilized HeNe laser (the fringe-offset technique [17]). The HeNe already available at IGISOL could be used for this, but first the long-term stability must be verified.

Appendix A

Saturation spectra

In this appendix all saturation spectra fitted with a hyperfine structure with a parabolic background and free intensities are shown. The top panel each time is the spectrum with the background fit in green and the total fit in red. The middle panel is only the fitted hyperfine structure, the background is subtracted. The bottom panel are the residuals.

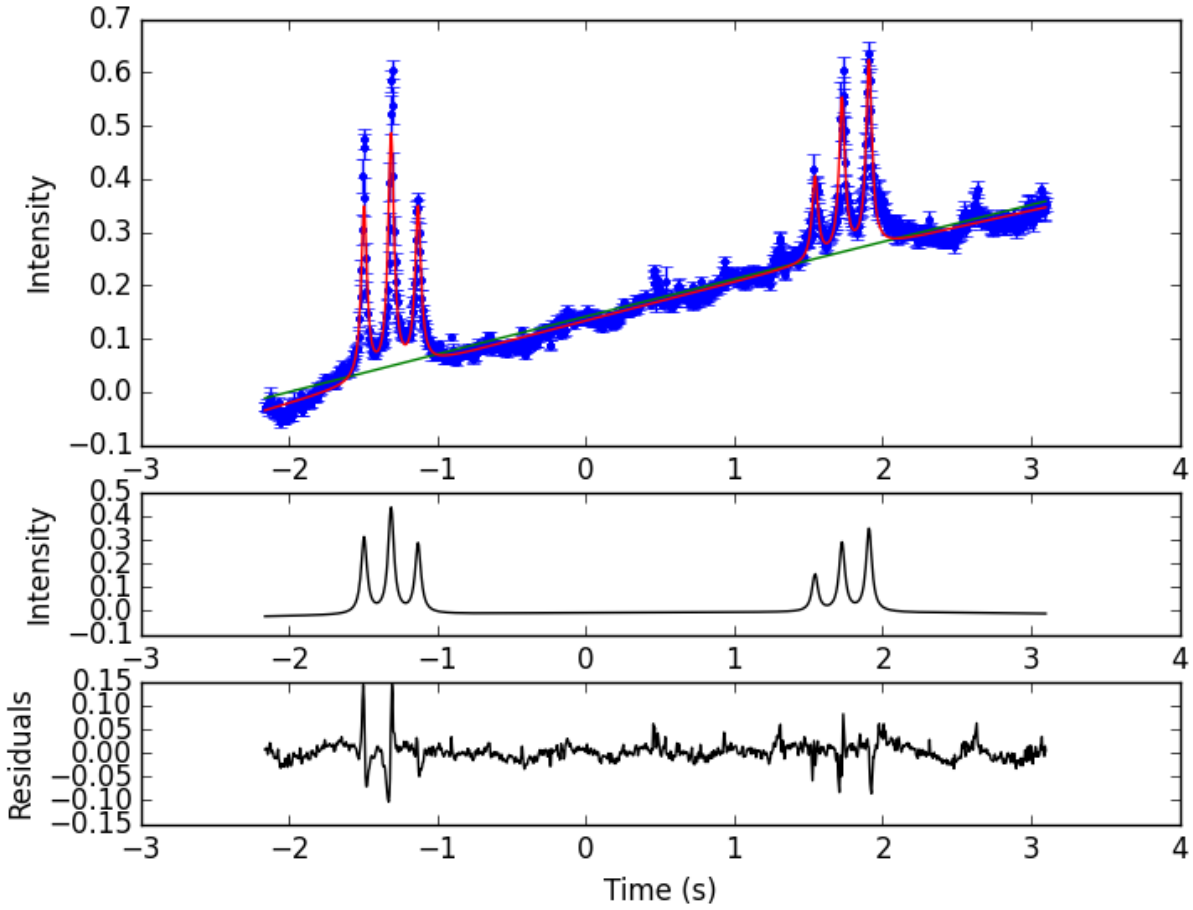

Figure A.1: First scan.

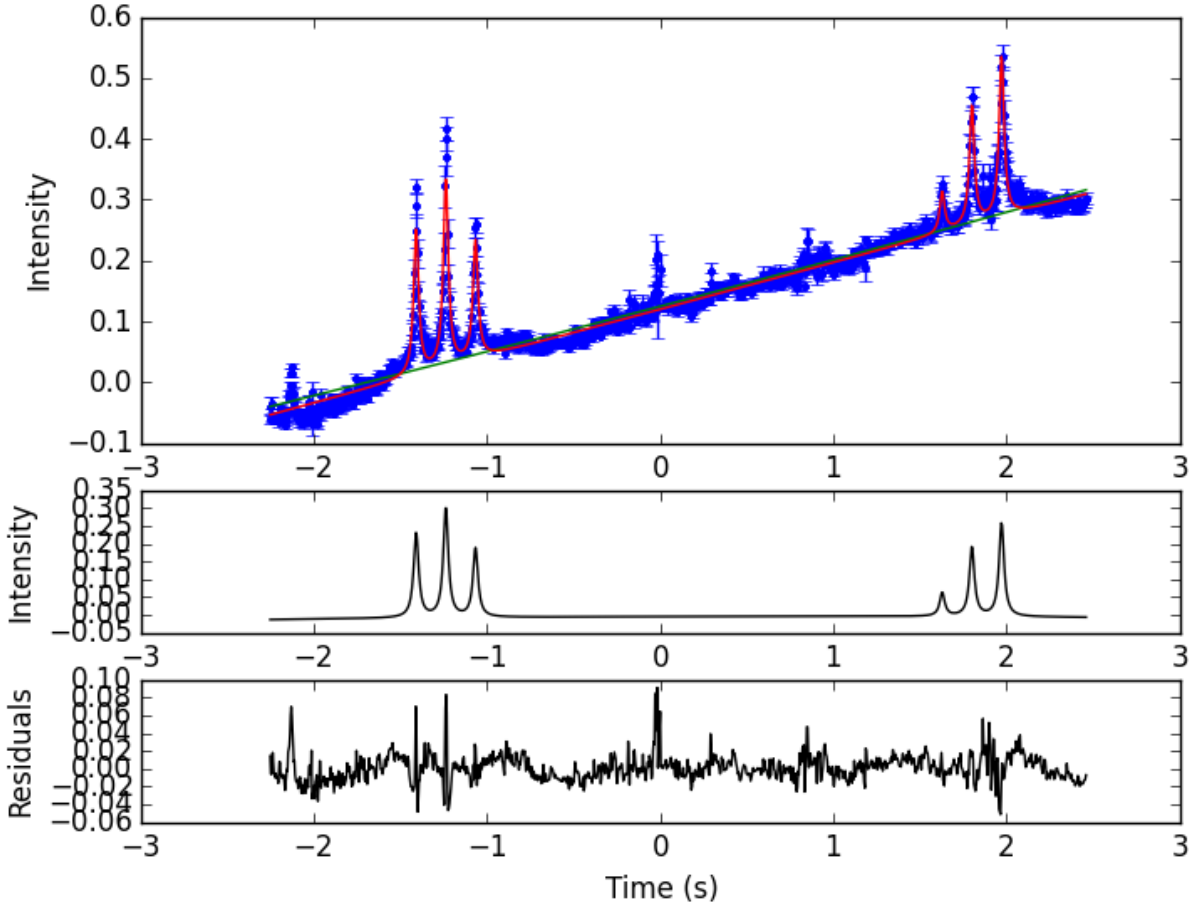

Figure A.2: Second scan.

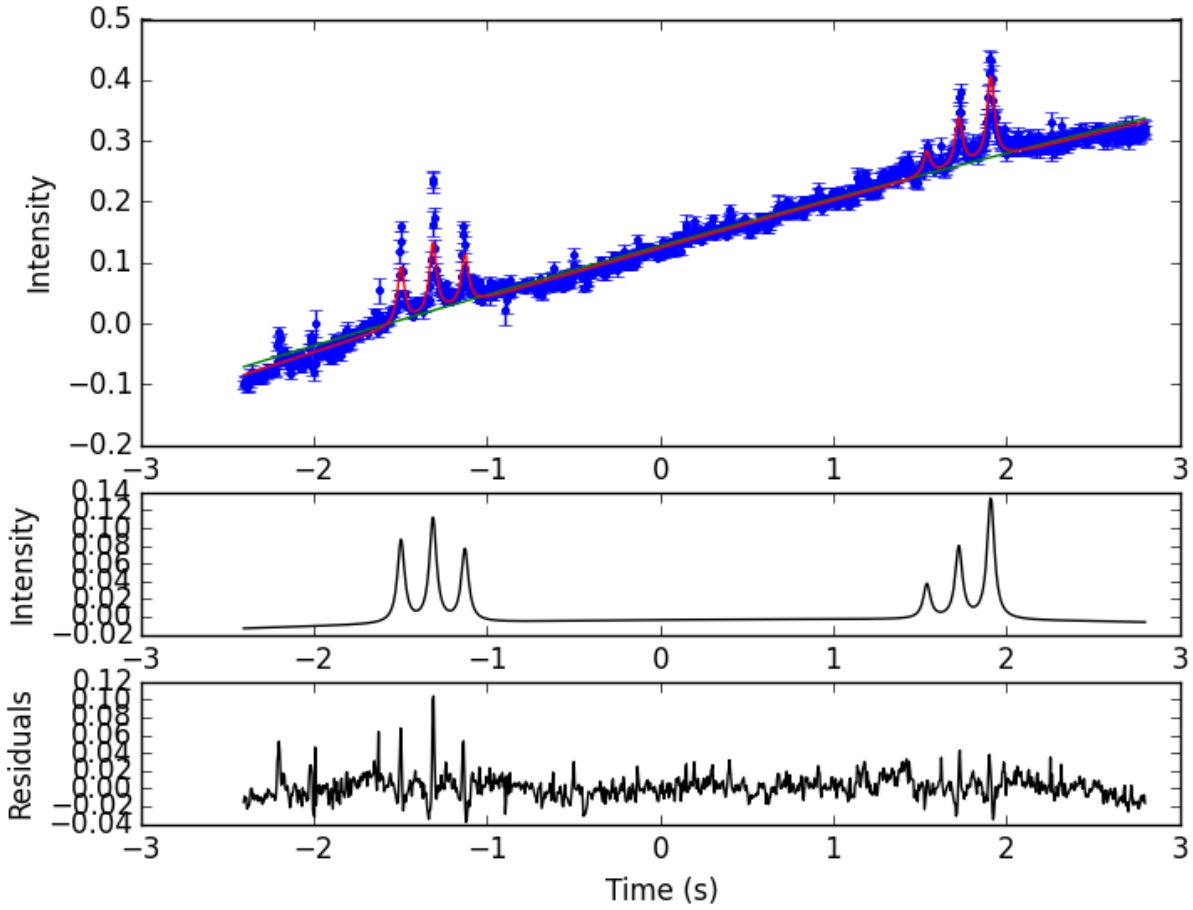

Figure A.3: Third scan.

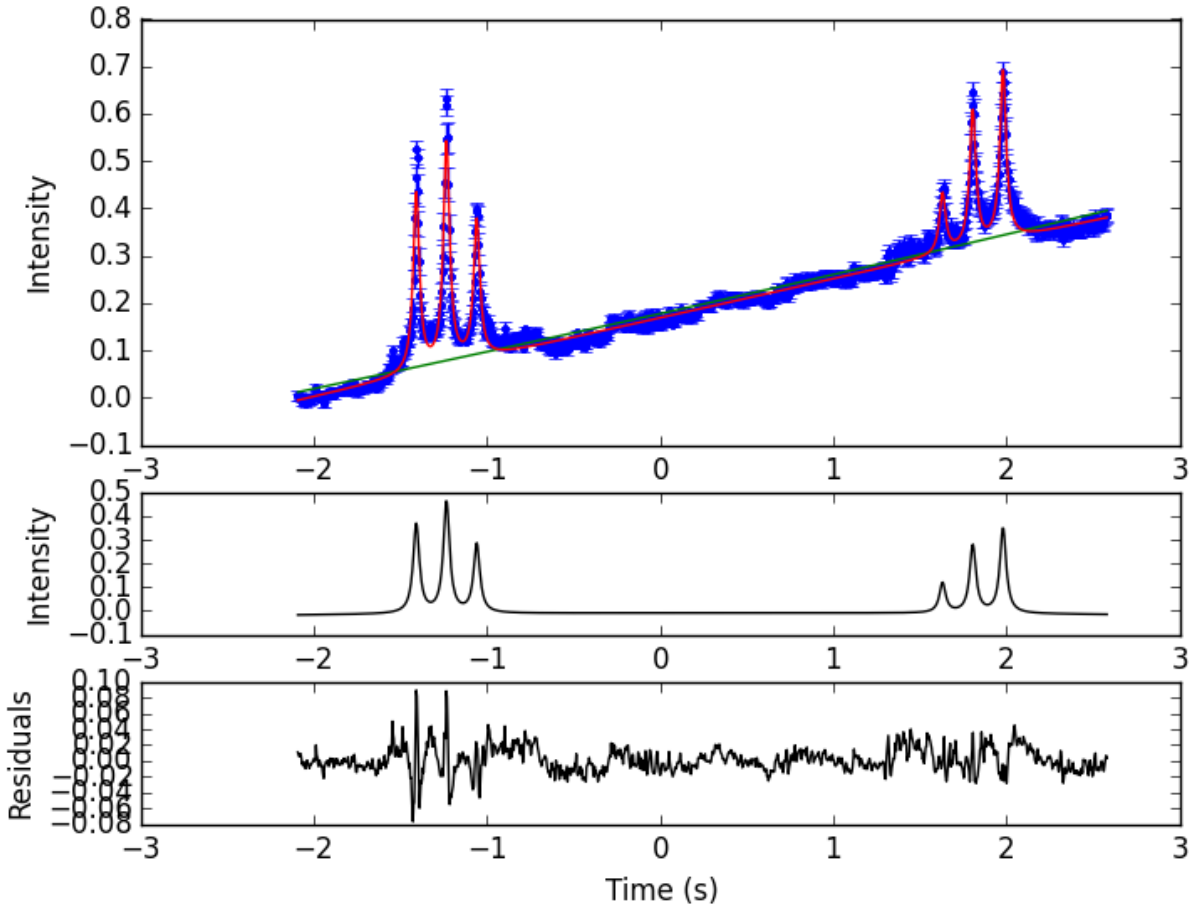

Figure A.4: Fourth scan.

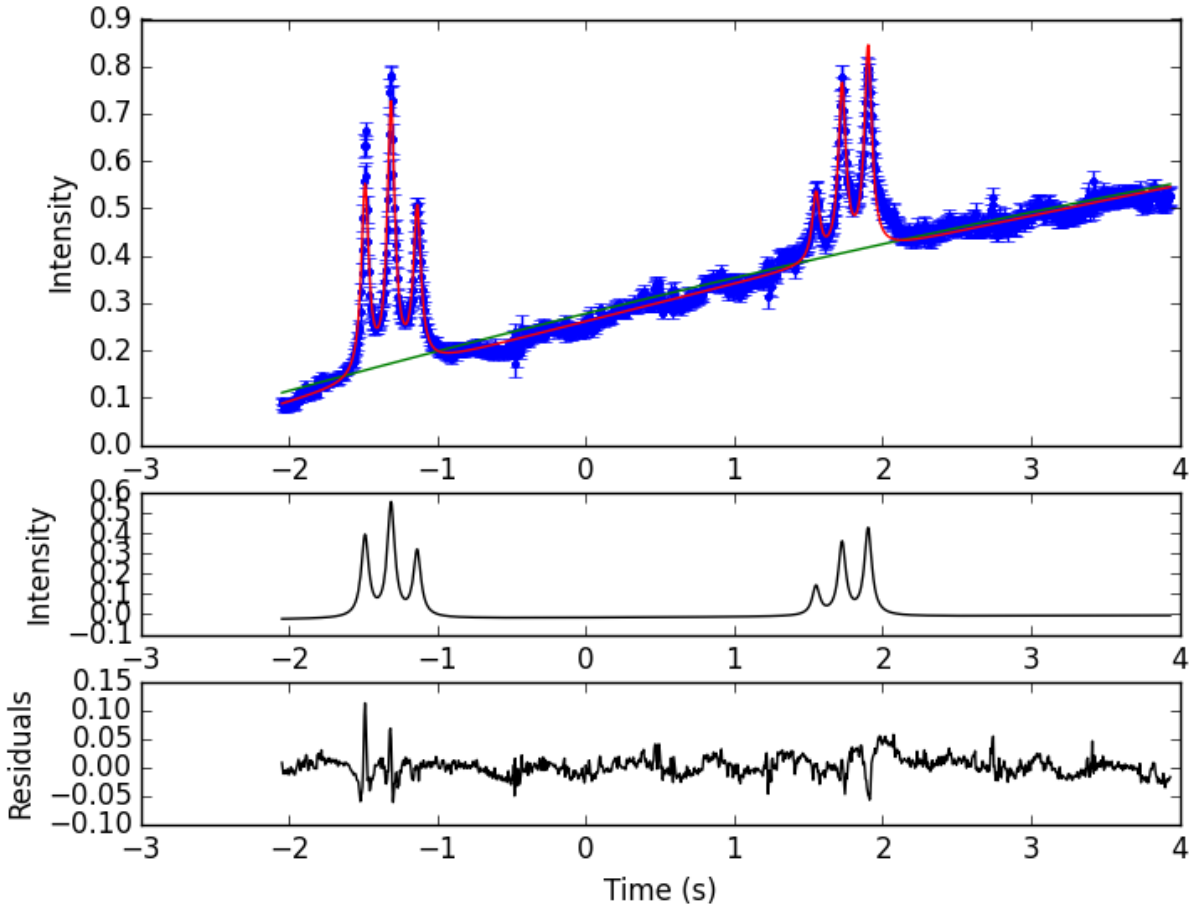

Figure A.5: Fifth scan.

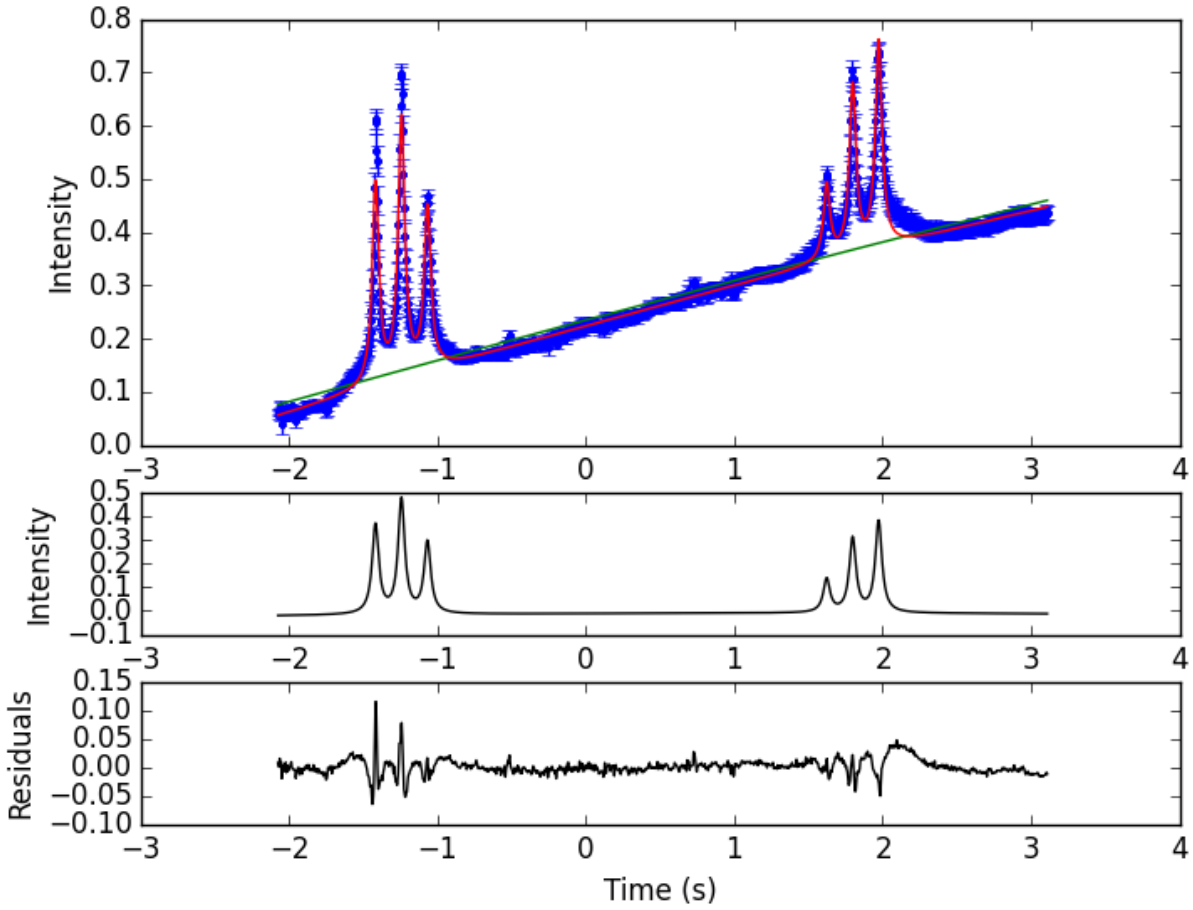

Figure A.6: Sixth scan.

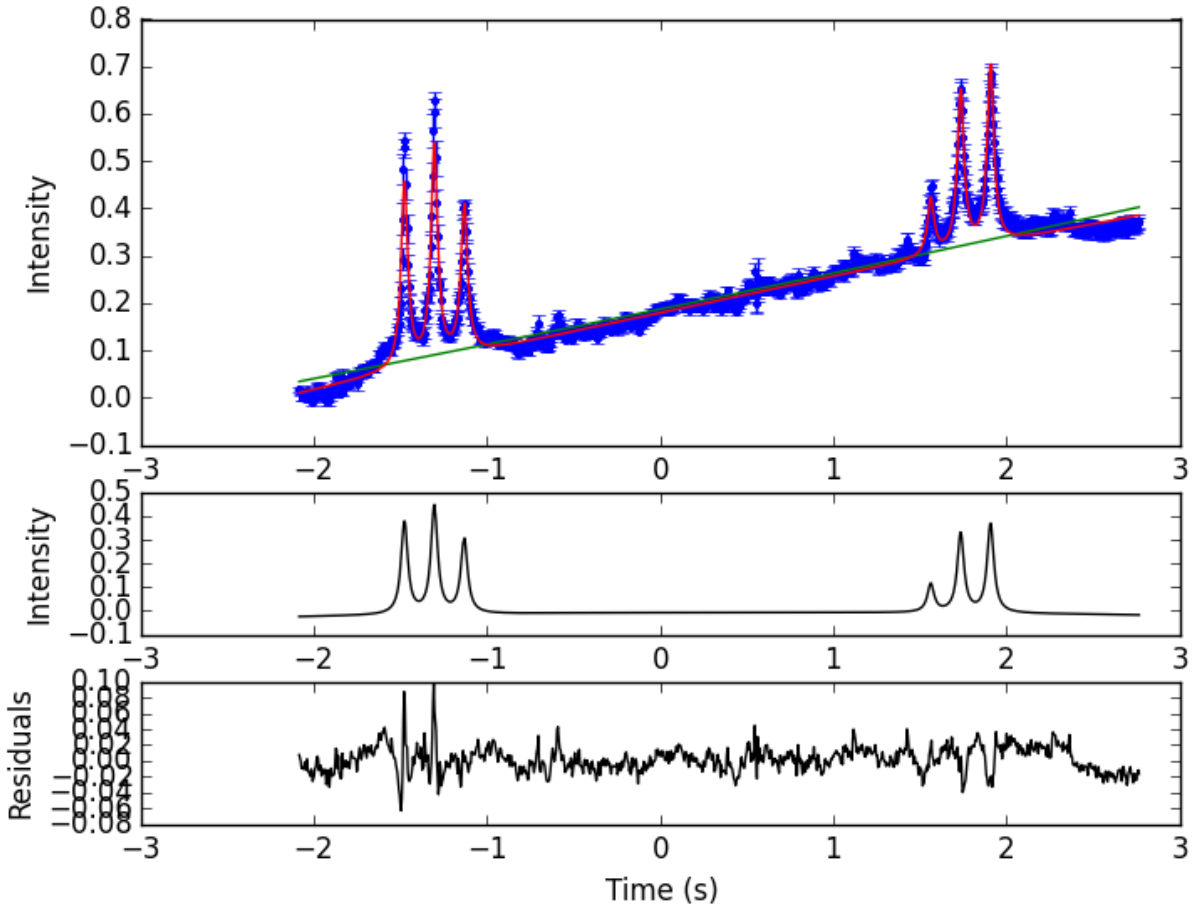

Figure A.7: Seventh scan.

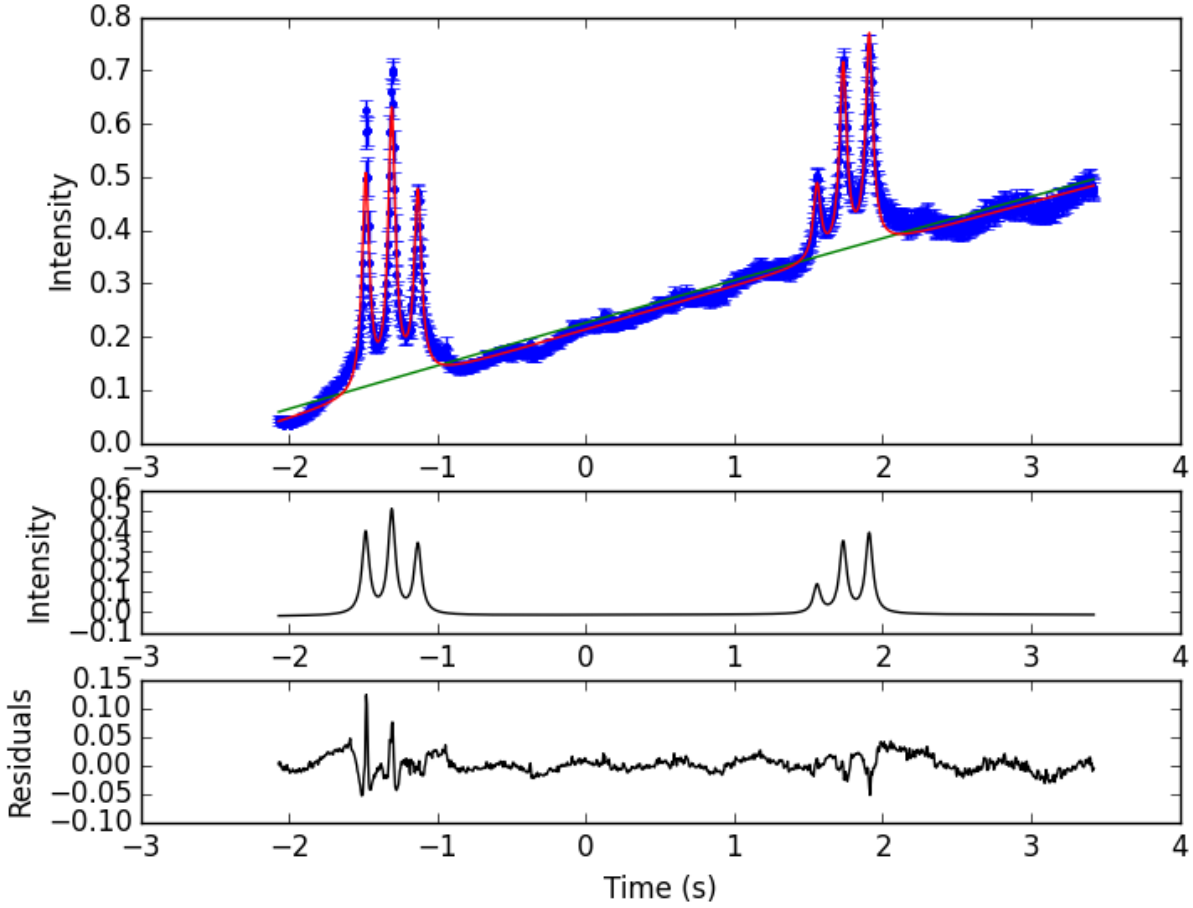

Figure A.8: Eighth scan.

Bibliography

[1] Wolfgang Demtröder, *Laser spectroscopy*, Fifth edition (volume 1 and 2), Springer, 2014.

[2] R. Neugart and G. Neyens, *Nuclear Moments*, Lect. Notes Phys. 700, p. 135-189, 2006.

[3] D. H. Forrest and B. Cheal, *Physics highlights from laser spectroscopy at the IGISOL*, Hyp Int 223, p. 207-222, 2014.

[4] Avgoulea M et al., *Nuclear charge radii and electromagnetic moments of radioactive scandium isotopes and isomers*, J. Phys. G: Nucl. Part. Phys. 38, 025104, 2011.

[5] D. A. Steck. *Rubidium 85 D Line Data*, URL: http://steck.us/alkalidata/rubidium85numbers.pdf, accessed on 2015-06-07.

[6] D. A. Steck. *Rubidium 87 D Line Data*, URL: http://steck.us/alkalidata/rubidium87numbers.pdf, accessed on 2015-06-07.

[7] V. Sonnenschein, *Laser developments and high resolution resonance ionization spectroscopy of actinide elements*, PhD thesis, University of Jyväskylä, 2014.

[8] M. Eichhorn, *Laser Physics: From Principles to Practical Work in the Lab*, Graduate Texts in Physics, Springer, 2014.

[9] T.F. Johnston, *Design and performance of broadband optical diode to enforce one direction traveling wave operation of a ring laser*, IEEE J. QE-16, 483, 1980.

[10] S. Hooker and C. Webb, *Laser Physics*, Oxford University Press, 2010.

[11] T. H. Maiman, *Stimulated optical radiation in ruby*, Nature 187, 1960, p. 493-94.

[12] G. W. F. Drake, *Springer Handbook of Atomic, Molecular, and Optical physics*, p. 253-260, Springer, 2006.

[13] R. Paschotta, *Encyclopedia of Laser Physics and Technology*, URL: http://www.rp-photonics.com/encyclopedia.html, accessed on 2015-05-05.

[14] V.S. Letokhov and V.P. Chebotayev, *Nonlinear Laser Spectroscopy*, Springer Ser. Opt. Sci., Vol. 4, Springer, 1977.

[15] H. Penttilä, *The layout of the IGISOL 3 Facility*, Hyp. Int. 223, p. 5-16, 2014.

[16] P. Campbell et al., *First results from laser spectroscopy on bunched radioactive beams from the JYFL ion-beam cooler*, Eur. J. Phys. A 15, p. 45-48, 2002.

[17] W.Z. Zhao et al., *A computer-based digital feedback control of frequency drift of multiple lasers*, Review of Scientific Instruments 69(11), p. 3737-3740, 1998.

[18] URL: http://www.sirah.com/laser/cw-ring-lasers/matisse-ts, accessed on 2015-06-07.

[19] C. Scholl et al., *New spin assignments in the odd-odd $N = Z$ nucleus ^{42}Sc and the breaking of the ^{40}Ca core*, Phys. Rev. C 75, 064321, 2007.

[20] URL: http://www.toptica.com/products/photonicals/scanning_fabry_perot_interferometer_and_detector_unit.html, accessed on 2015-06-07.

[21] B. Singh and J.A. Cameron, Nucl. Data Sheets 92, 1, 2001.

[22] A.F. LisetskiyB. Singh and , *Magnetic dipole probes of the sd and pf shell crossing in the $^{36,38}Ar$ isotopes*, Nuclear Physics A 789, p. 114-124, 2007.

[23] M. L. Bissell et al., *Proton-Neutron Pairing Correlations in the Self-Conjugate Nucleus ^{38}K Probed via a Direct Measurement of the Isomer Shift*, Phys. Rev. Lett. 113, 052502, 2014.

[24] K. Krane, *Introductory Nuclear Physics*, John Wiley & Sons, 1998.

[25] J. Äystö et al., editors, *Three decades of research using IGISOL technique at the University of Jyväskylä*, Springer Netherlands, 2014.

[26] J. Ärje et al., *Ion Guide method for on-line isotope separation*, Nucl. Instrum. Methods Phys. Res. B 26, p. 384-393, 1987.

[27] P. Karvonen et al., *A sextupole ion beam guide to improve the efficiency and beam quality at IGISOL*, Nucl. Instrum. Methods Phys. Res. B 266, p. 4794-4807, 2008.

[28] T. Kessler et al., *Off-line studies of the laser ionization of yttrium at the IGISOL facility*, Nucl. Instrum. Methods Phys. Res. B 266, p. 681-700, 2008.

[29] M. Reponen et al., *Gas jet studies towards an optimization of the IGISOL LIST method*, Nucl. Instrum. Methods Phys. Res. A 635, p. 24-34, 2011.

[30] P. Karvonen et al., *LIST developments at IGISOL*, The European Physical Journal Special Topics 150, p. 283-284, 2007.

[31] A. Nieminen et al., *On-Line Ion Cooling and Bunching for Collinear Laser Spectroscopy*, Phys. Rev. Lett. 88(9), 094801, 2002.

[32] K. Baczynska et al., *Nuclear spin determination of ^{100m}Y by collinear laser spectroscopy of optically pumped ions*, J. Phys. G: Nucl. Part. Phys. 37, 105103, 2010.

[33] R. Moore et al., *Character of an 8^- isomer of ^{130}Ba*, Phys. Lett. B 547, p. 200-204, 2002.

[34] I. Budinčević et al., *Laser spectroscopy of francium isotopes at the borders of the region of reflection asymmetry*, Phys. Rev. C 90, 014317, 2014.

[35] T. Eronen et al., *JYFLTRAP: a Penning trap for precision mass spectroscopy and isobaric purification*, Eur. Phys. J. A 48(4), p. 1-21, 2012.

[36] M. Mayer and J. H. D. Jensen, *Elementary Theory of Nuclear Shell Structure*, Wiley, 1995.

[37] A. Einstein, *Zur Quantentheorie der Strahlung*, Physikalische Zeitschrift 18, p. 121-128, 1917.

[38] J. M. G. Levins et al., *First On-Line Laser Spectroscopy of Radioisotopes of a Refractory Element*, Phys. Rev. Lett. 82, p. 2476-2479, 1992.

[39] M.L. Bissell et al., *On the decrease in charge radii of multi-quasi particle isomers*, Phys. Lett. B 645, p. 330-334, 2007.

[40] URL: http://cars9.uchicago.edu/software/python/lmfit/, accessed on 2015-06-07.

[41] R. J. Barlow, *Statistics: A Guide to the Use of Statistical Methods in the Physical Sciences*, Wiley, 1989.

AFDELING
Straat nr bus 0000
3000 LEUVEN, BELGIË
tel. + 32 16 00 00 00
fax + 32 16 00 00 00
www.kuleuven.be